Multiresolution Analysis Based on Dual-Scale Regression for Pansharpening

Peng Wang, *Member, IEEE*, Hongyu Yao, Cai Li, Gong Zhang, *Member, IEEE*, and Henry Leung, *Fellow, IEEE*

***Abstract*—Pansharpening technique is used to merge the original multispectral image (MS) with a high spatial resolution panchromatic image (PAN). Due to its robustness, the multiresolution analysis (MRA) is an important part of pansharpening. The scale regression model is effective for improving MRA. However, the existing MRA based on scale regression results into single-scale regression information, thus affecting the final pansharpening result. To address this problem, in this work, we propose a dual-scale regression-based MRA for pansharpening. First, we establish a scale regression-based model. Then, this model is improved using a high-pass modulation (HPM) injection scheme. Finally, the dual-scale information is added to the scale regression to construct the dual-scale regression for obtaining the final pansharpening result. We perform experiments using five datasets. The results show that the proposed method obtains a better pansharpening result as compared to various state-of-the-art MRA methods. In addition, the quantitative and qualitative analysis of the results shows that the proposed method achieves appropriate spatial and spectral resolution fusion. Therefore, it has a great potential in pansharpening technique.**

***Index Terms*—Dual scale regression, multiresolution analysis (MRA), multispectral image (MS), panchromatic image (PAN), pansharpening.**

Manuscript received September 21, 2021; revised November 18, 2021; accepted November 26, 2021. Date of publication November 30, 2021; date of current version February 21, 2022. This work was supported in part by the National Natural Science Foundation of China under Grant 61801211; in part by the Fundamental Research Funds for the Central Universities in the Nanjing University of Aeronautics and Astronautics under Grant NZ2020009; in part by the Open Project Program of Hubei Key Laboratory of Regional Development and Environment Response Fundamental under Grant 2020(B)004; in part by the Open Project Program of State Key Laboratory of Tropical Oceanography, South China Sea Institute of Oceanology, Chinese Academy of Sciences under Grant LTO2118; in part by the Foundation of Graduate Innovation Center in the Nanjing University of Aeronautics and Astronautics under Grant xcxjh20210405; in part by the Graduate Education and Teaching Reform Research Project in the Nanjing University of Aeronautics and Astronautics under Grant 2021YJXGG11; and in part by the Open Research Project of Hubei Key Laboratory of Intelligent Geo-Information Processing under Grant KLIGIP-2019A05. *(Corresponding author: Peng Wang.)*

Peng Wang is with the Key Laboratory of Radar Imaging and Microwave Photonics, Ministry of Education, Nanjing University of Aeronautics and Astronautics, Nanjing 210016, China, and also with the Hubei Key Laboratory of Regional Development and Environment Response, Hubei University, Hubei 430062, China (e-mail: pengwang-B614080003@hotmail.com).

Hongyu Yao and Gong Zhang are with the Key Laboratory of Radar Imaging and Microwave Photonics, Ministry of Education, Nanjing University of Aeronautics and Astronautics, Nanjing 210016, China.

Cai Li is with the State Key Laboratory of Tropical Oceanography, South China Sea Institute of Oceanology, Chinese Academy of Sciences, Guangzhou, Guangdong 510301, China.

Henry Leung is with the Department of Electrical and Computer Engineering, University of Calgary, Calgary, AB T2N 1N4, Canada.

Digital Object Identifier 10.1109/TGRS.2021.3131477

Nomenclature

MS	Multispectral image.
PAN	Panchromatic image.
CS	Component substitution.
MRA	Multiresolution analysis.
HPM	High-pass modulation.
MTF	Modulation-transfer function.
GLP	Generalized Laplacian pyramid.
P^{LR}	Low-resolution PAN image.
P^{HR}	High-resolution PAN image.
M_b^{LR}	Low-resolution MS image.
M_b^{HR}	High-/Low-resolution MS image.
$\hat{M}_b^{\mathrm{LR}}$	M_b^{LR} interpolated to the size of P^{HR}.
ERGAS	Relative dimensionless global error in synthesis.
SAM	Spectral angle mapper.
$Q2^n$	2^n bands is the Universal Image Quality Index.
D_λ	Spectral distortion.
D_S	Spatial distortion.
QNR	Quality no-reference.

I. Introduction

PHYSICAL limitations and processing capabilities of satellite remote-sensing equipment hinder a single sensor from collecting the remote sensing images with high spatial and spectral resolutions simultaneously [1]. The MS images have rich spectral information, but a continuous improvement in the spectral resolution of MS images affects their spatial resolution. Remote-sensing image processing has developed many topics, such as super-resolution [2]–[4], feature extraction [5], cloud removal [6], and classification [7]. In addition, the pansharpening technique [8]–[10] has been proposed to improve the spatial resolution of an MS image using a high spatial resolution PAN image. Pansharpening has important applications in environmental monitoring, land and resource use, precision agriculture, urban planning, military reconnaissance, and other key areas.

Currently, the common pansharpening methods can be categorized into three types [11], [12], including component CS, MRA, and deep learning [13]. The CS methods include intensity-hue-saturation [14], principal component analysis [15], Gram-Schmidt [16], and adaptive GS [17]. Although the CS methods usually have a simple physical meaning and high-computational efficiency, the pansharpening results differ from the ideal output. Recently, the deep learning-based techniques have been applied to pansharpening, including pansharpening neural network [18]–[20] and its complex variations in terms of network depth [21]–[23], topology [24], [25], and fine-tuning [26], [27]. Although the deep learning-based methods achieve better performance as compared to the traditional machine learning methods, such as CS- and MRA-based methods, the deep learning usually requires a large amount of labeled training data to achieve the desired performance. In addition to the above three types, geostatistics-based technique is also an effective solution to the pansharpening problem, such as area-to-point regression kriging [28] and the information loss-guided image fusion [29].

The MRA-based methods inject spatial information in the MS images. Since the MRA methods do not require the training data and are more effective in retaining the spectral characteristics of the original MS image than the CS, they have been relatively successful and popular for implementing pansharpening techniques [2]. The MRA-based methods include the additive wavelet luminance proportional (AWLP) [30], smoothing filter based on intensity modulation (SFIM) [31], and morphological filters (MF) [32]. In addition, the GLP based on Gaussian filters matches the MTF of an MS sensor (MTF-GLP) [33]. It is notable that the MTF-GLP has been successfully applied to the MRA. The MTF-GLP with a context-based decision (MTF-GLP-CBD) [34], context-adaptive MTF-GLP-CBD (C-MTF-GLP-CBD) [35], MTF-GLP with HPM (MTF-GLP-HPM) [36], [37], MTF-GLP-HPM based on haze-corrected version (MTF-GLP-HPM-H) [38], and MTF-GLP-HPM based on post-processing (MTF-GLP-HPM-PP) [39] belong to MAR based on the MTF-GLP technique. The scale regression model is effective for improving the MRA and obtaining better results. The scale regression model [40] is a mathematical model that quantitatively describes the statistical relationships. This indicates the influence and significant relationship between the independent and dependent variables. Some of the MRA methods are based on scale regression methods, including the MTF-GLP based on full-scale regression (MTF-GLP-REG-FS) [41] and MTF-GLP-HPM based on multivariate linear regression (MTF-GLP-HPM-R) [42].

However, the existing MRA methods based on scale regression suffer from insufficient scale regression information, which affects the pansharpening result. To overcome this problem, in this work, we propose an MRA method based on dual-scale regression for pansharpening method, namely MTF-GLP-HPM-DS. The proposed method improves the accuracy of pansharpening and promotes wider application of pansharpening. We aim to solve the issue of scale regression information based on MRA pansharpening. In the proposed method, first, a scale regression-based MRA model is designed. Then, this model is improved using the HPM injection scheme. Finally, the dual-scale information, including the fine-scale and coarse-scale information, are added to the scale regression to obtain the final pansharpening result. The experimental results show the superiority of the proposed MTF-GLP-HPM-DS over various state-of-the-art MRA methods.

The contributions of this article are summarized below.

1) The dual-scale regression model uses abundant scale regression information, which improves the pansharpening result.
2) In the dual-scale regression model, the fine-scale and coarse-scale information are linked by a parameter that can be adjusted to make the proposed method adaptive for different scenarios, unlike the existing MRA methods.
3) We show that the dual-scale regression model is feasible in terms of mathematical analysis and experiments.

The remaining of this article is organized as follows.

The proposed method is described in Section II. The experimental results and comparisons of the proposed method with state-of-the-art methods are presented in Section III. The discussion of the results is presented in Section IV. Finally, the conclusion is drawn in Section V.

II. Methodology

A. Scale Regression-Based MRA Model

Let P^{HR} be a high-resolution PAN image with a size of $M \times N$, where N and M represent the numbers of rows and columns of the PAN image, respectively. The low-resolution MS image $M^{\mathrm{LR}} = \{M^{\mathrm{LR}}\}_{b=1,\ldots,B}$ has a size of $M/S \times N/S$ and B spectral bands, where M_b^{LR} represents the bth spectral band and S denotes the ratio scale between P^{HR} and M^{LR}. Furthermore, the superscript denotes the spatial resolution of an image; i.e., LR and HR represent low and high resolutions, respectively.

The MRA model is used in this article. First, M^{LR} is interpolated to the size of P^{HR}, producing $\hat{M}^{\mathrm{LR}} = \{\hat{M}^{\mathrm{LR}}\}_{b=1,\ldots,B}$. Then, the MTF-GLP [33] is used to obtain a low-pass version of the LR-PAN image, i.e., P^{LR}, from P^{HR}. In this work, we use the MTF filter for down-sampling. This filter is a Gaussian filter matched with the MTF of the MS sensor [33]. Finally, the injection coefficients g are used to control the difference in information injection, as shown in (1), and the pansharpening result $M^{\mathrm{HR}} = \{M^{\mathrm{HR}}\}_{b=1,\ldots,B}$ is obtained.

Based on [4], the MRA for the bth spectral band is equivalent to expressions presented in (1)–(3)

$$M_b^{\mathrm{HR}} = \hat{M}_b^{\mathrm{LR}} + g_b\left(P^{\mathrm{HR}} - P^{\mathrm{LR}}\right) \tag{1}$$

$$P^{\mathrm{LR}} = P^{\mathrm{HR}} * h \tag{2}$$

where, h denotes the MTF filter, g_b denotes the injection coefficients for the bth spectral band of an MS image, and is defined as follows:

$$g_b = \frac{\mathrm{cov}\left(\hat{M}_b^{\mathrm{LR}}, P^{\mathrm{LR}}\right)}{\mathrm{var}\left(P^{\mathrm{LR}}\right)} \tag{3}$$

where, $\mathrm{cov}(A, B)$ denotes the covariance of, and $\mathrm{var}(A)$ denotes the sample variance of image A.

Based on [4], another pansharpening-type CS is equivalent to the expressions presented in (4)–(6)

$$M_b^{\mathrm{HR}} = \hat{M}_b^{\mathrm{LR}} + g_b\big(P^{\mathrm{HR}} - I^{\mathrm{LR}}\big) \tag{4}$$

$$I^{\mathrm{LR}} = \sum_{b=1}^{B} w_b \hat{M}_b^{\mathrm{LR}} \tag{5}$$

$$g_b = \frac{\mathrm{cov}\big(\hat{M}_b^{\mathrm{LR}}, I^{\mathrm{LR}}\big)}{\mathrm{var}\big(I^{\mathrm{LR}}\big)} \tag{6}$$

where $\{w_b\}_{b=1,\ldots,B}$ can be estimated by computing minimum mean square error (MMSE). The intensity component I^{LR} is a function of the MS image. Therefore, the procedure between MRA and CS is different.

In this work, a scale regression-based MRA model is designed. In the proposed model, the full-scale regression [41] is used to obtain the appropriate injection coefficients g_b iteratively. Based on [41], the assumption of scale invariance is used to replace the low-resolution P^{LR} with high-resolution P^{HR}. The high-resolution MS M_b^{HR} and injection coefficients g_b are used to perform iterative operations. Therefore, (3) can be rewritten as follows:

$$g_b^i = \frac{\mathrm{cov}\Big(M_b^{\mathrm{HR},i}, P^{\mathrm{HR}}\Big)}{\mathrm{var}\big(P^{\mathrm{HR}}\big)}. \tag{7}$$

The specific iterative operations are presented in Algorithm 1. First, the initial injection coefficients g_b^0 are obtained for $M_b^{\mathrm{HR},0} = \hat{M}_b^{\mathrm{LR}}$. Then, multiple iterations are performed to obtain the injection coefficients g_b. Finally, the iterative process is stopped when the convergence is achieved.

Algorithm 1: Iterative Procedure

for $i = 0, \ldots, N-1$ **do**

- Injection coefficients calculation g_b^i

$$g_b^i = \frac{\mathrm{cov}\Big(M_b^{\mathrm{HR},i}, P^{\mathrm{HR}}\Big)}{\mathrm{var}\big(P^{\mathrm{HR}}\big)}.$$

- Using g_b^i to fuse MS and PAN

$$M_b^{\mathrm{HR},i+1} = \hat{M}_b^{\mathrm{LR}} + g_b^i\big(P^{\mathrm{HR}} - P^{\mathrm{LR}}\big).$$

end

B. HPM Injection Scheme

The HPM injection scheme improves the MRA [34], [35], so it is employed in this work to improve the performance of an MRA model based on scale regression.

According to the HPM injection scheme, (1) can be rewritten as

$$M_b^{\mathrm{HR}} = \hat{M}_b^{\mathrm{LR}} \frac{P^{\mathrm{HR}}}{P^{\mathrm{LR}}}. \tag{8}$$

Now, we explain the process of adding the scale regression to the HPM injection scheme. A digital MS or PAN image N_s^{XR} acquired by a sensor s is defined as a convolution of the sensor spatial response and the total energy collected by the sensor in its spectral band [43], [44] as

$$\begin{aligned} N_s^{\mathrm{XR}}(x,y) &= \delta_s + k_s \int_{-\infty}^{+\infty}\int_{-\infty}^{+\infty} S_s(x-\alpha, y-\beta) \\ &\quad \cdot \left(\int_{-\infty}^{+\infty} E_s(\alpha,\beta,\lambda) R_s(\lambda) d\lambda\right) d\alpha d\beta \\ &= \delta_s + k_s S_s^{\mathrm{XR}} * W_s \end{aligned} \tag{9}$$

where, the superscript XR either denotes HR or LR, δ_s represents an additive constant, and k_s represents a multiplicative constant. x and y denote the pixel coordinates.

The two constants are introduced to obtain the complete digital range of the A/D converter; however, δ_s is usually negligible. Furthermore, S_s denotes the spatial response of sensor s, and W_s represents the integral over the frequency λ of the at-sensor radiance $E_s(\alpha, y, \lambda)$ weighted by the relative spectral response $R_s(\lambda)$ [45], and is obtained as

$$W_s = \int_{-\infty}^{+\infty} E_s(\alpha, y, \lambda) d\lambda. \tag{10}$$

Based on (8) and (9), $\hat{M}_b^{\mathrm{LR}}$, P^{LR}, and P^{HR} are now expressed as follows:

$$\hat{M}_b^{\mathrm{LR}} = k_b S_b^{\mathrm{LR}} * W_b \tag{11}$$

$$P^{\mathrm{LR}} = k_p S_p^{\mathrm{LR}} * W_p \tag{12}$$

$$P^{\mathrm{HR}} = k_p S_p^{\mathrm{HR}} * W_p \tag{13}$$

where, S_b^{LR}, S_p^{LR}, and S_p^{HR} denote the spatial responses of LR-MS, LR-PAN, and HR-PAN images, respectively; W_b and W_p represent the total energies of MS and PAN images, respectively; k_b and k_p denote the multiplicative constants.

Thus, the aim of pansharpening is to obtain a high-resolution MS image M_b^{HR} that has the spatial response HR-PAN S_p^{HR} and the total energy W_b. The target expression of M_b^{HR} is defined as

$$M_b^{\mathrm{HR}} = k_b S_p^{\mathrm{HR}} * W_b. \tag{14}$$

Considering the HPM injection scheme, (11)–(13) are substituted into (8), and M_b^{HR} is obtained as follows:

$$M_b^{\mathrm{HR}} = \big(k_b S_b^{\mathrm{LR}} * W_b\big) \frac{k_p S_p^{\mathrm{HR}} * W_p}{k_p S_p^{\mathrm{LR}} * W_p}. \tag{15}$$

This can be converted to the target expression, i.e., (14), by appropriately setting the multiplication coefficients of $\hat{M}_b^{\mathrm{LR}}$. This indicates that the variables except $\hat{M}_b^{\mathrm{LR}}$ are different from (15). Therefore, these variables are expressed using an additional tilde to differentiate between the actual and estimated variables.

Therefore, the modified equation is given as

$$\tilde{M}_b^{\mathrm{HR}} = \hat{M}_b^{\mathrm{LR}} \frac{\tilde{P}^{\mathrm{HR}}}{\tilde{P}^{\mathrm{LR}}} = \big(k_b S_b^{\mathrm{LR}} * W_b\big) \frac{k_p \tilde{S}_p^{\mathrm{HR}} * \tilde{W}_p}{k_p \tilde{S}_p^{\mathrm{LR}} * \tilde{W}_p}. \tag{16}$$

Now, the desired result is obtained by deriving the following equalities. Since the spatial response of the HR-MS sensor should be the same as that of the existing PAN camera, the first equality is expressed as

$$\tilde{S}_p^{\mathrm{HR}} = S_p^{\mathrm{HR}}. \tag{17}$$

Furthermore, since the LR-PAN image P^{LR} is constructed by the MTF-GLP, which utilizes a filter to match the spatial response of the LR-MS sensor, the second equality is defined as follows:

$$\tilde{S}_p^{\mathrm{LR}} = S_b^{\mathrm{LR}}. \tag{18}$$

Based on [42], the third equality is defined as

$$k_p \tilde{W}_p = k_b W_b. \tag{19}$$

Thus, considering (11) and (12), we obtain (20)

$$\begin{aligned}\tilde{P}^{\mathrm{LR}} &= k_p \tilde{S}_p^{\mathrm{LR}} * \tilde{W}_p \\ &= k_b S_b^{\mathrm{LR}} * W_b \\ &= \hat{M}_b^{\mathrm{LR}}.\end{aligned} \tag{20}$$

Similarly, considering (13) and (14), we obtain (21)

$$\begin{aligned}\tilde{P}^{\mathrm{HR}} &= k_p \tilde{S}_p^{\mathrm{HR}} * \tilde{W}_p \\ &= k_b S_p^{\mathrm{HR}} * W_b \\ &= M_b^{\mathrm{HR}}.\end{aligned} \tag{21}$$

Based on (20) and (21), a linear affine function is proposed to solve M_b^{XR}, and is mathematically expressed as

$$\tilde{P}^{\mathrm{XR}} = m P^{\mathrm{XR}} + n = M_b^{\mathrm{XR}}. \tag{22}$$

Thus, the problem is transformed into the problem of finding coefficients m and n to obtain M_b^{XR}. In this work, the spectral matching based on scale regression between the HR-PAN image and HR-MS image is used to compute the coefficients m and n [42] as follows:

$$m = \frac{\mathrm{cov}\left(M_b^{\mathrm{HR}}, P^{\mathrm{HR}}\right)}{\mathrm{var}\left(P^{\mathrm{HR}}\right)} \tag{23}$$

$$n = \mathrm{E}\left(M_b^{\mathrm{HR}}\right) - \frac{\mathrm{cov}\left(M_b^{\mathrm{HR}}, P^{\mathrm{HR}}\right)}{\mathrm{var}\left(P^{\mathrm{HR}}\right)} \mathrm{E}\left(P^{\mathrm{HR}}\right) \tag{24}$$

where, $E(X)$ represents the mean of image X.

Therefore, we rewrite (16) as follows:

$$\begin{aligned}M_b^{\mathrm{HR}} &= \hat{M}_b^{\mathrm{LR}} \frac{\tilde{P}^{\mathrm{HR}}}{\tilde{P}^{\mathrm{LR}}} \\ &= \hat{M}_b^{\mathrm{LR}} \frac{P^{\mathrm{HR}} - \mathrm{E}\left(P^{\mathrm{HR}}\right) + \mathrm{E}\left(M_b^{\mathrm{HR}}\right) \Big/ \frac{\mathrm{cov}\left(M_b^{\mathrm{HR}}, P^{\mathrm{HR}}\right)}{\mathrm{var}\left(P^{\mathrm{HR}}\right)}}{P^{\mathrm{LR}} - \mathrm{E}\left(P^{\mathrm{HR}}\right) + \mathrm{E}\left(M_b^{\mathrm{HR}}\right) \Big/ \frac{\mathrm{cov}\left(M_b^{\mathrm{HR}}, P^{\mathrm{HR}}\right)}{\mathrm{var}\left(P^{\mathrm{HR}}\right)}}.\end{aligned} \tag{25}$$

According to the definition of the injection coefficients g_b based on the scale regression in (7), (25) can be written as follows:

$$M_b^{\mathrm{HR}} = \hat{M}_b^{\mathrm{LR}} \frac{P^{\mathrm{HR}} - \mathrm{E}\left(P^{\mathrm{HR}}\right) + \mathrm{E}\left(M_b^{\mathrm{HR}}\right)/g_b}{P^{\mathrm{LR}} - \mathrm{E}\left(P^{\mathrm{HR}}\right) + \mathrm{E}\left(M_b^{\mathrm{HR}}\right)/g_b}. \tag{26}$$

As presented in (26), the scale regression is successfully added to HPM injection scheme.

C. Dual-Scale Regression Model

According to (7), the injection coefficients g_b based on the scale regression only consider the covariance of P^{HR} at a fine scale and M_b^{HR}. Therefore, the scale regression information in g_b is single, which affects the performance of the proposed MRA based on the scale regression model. To enrich the scale information for scale regression and improve the final pansharpening results, the dual-scale information is introduced in the scale regression to construct the dual-scale regression. In other words, the proposed dual-scale regression not only considers the fine-scale information of the covariance between P^{HR} and M_b^{HR}, but also the coarse-scale information of the covariance between P^{LR} and M_b^{HR}. Thus, we obtain

$$g_b^i = \mu \frac{\mathrm{cov}\left(M_b^{\mathrm{HR},i}, P^{\mathrm{HR}}\right)}{\mathrm{var}\left(P^{\mathrm{HR}}\right)} + (1-\mu) \frac{\mathrm{cov}\left(M_b^{\mathrm{HR},i}, P^{\mathrm{LR}}\right)}{\mathrm{var}\left(P^{\mathrm{HR}}\right)} \tag{27}$$

where, μ is adjusted to make the proposed method more flexible in different scenarios. In this section, the final injection coefficients are introduced to realize the dual-scale regression iteratively. In addition, a closed-form solution of the iterative process is adopted, so that the iterative method achieves a considerable performance.

Now, we show that the dual-scale regression model is iterative and convergent. Appendix A demonstrates that the progress of the mathematical induction in detail. First, the initial injection coefficients g_b^0 are obtained for $M_b^{\mathrm{HR},0} = \hat{M}_b^{\mathrm{LR}}$ and is defined as

$$g_b^0 = \mu \frac{\mathrm{cov}\left(\hat{M}_b^{\mathrm{LR}}, P^{\mathrm{HR}}\right)}{\mathrm{var}\left(P^{\mathrm{HR}}\right)} + (1-\mu) \frac{\mathrm{cov}\left(\hat{M}_b^{\mathrm{LR}}, P^{\mathrm{LR}}\right)}{\mathrm{var}\left(P^{\mathrm{HR}}\right)}. \tag{28}$$

Thus, the expression of g_b^{n-1} is obtained as

$$\begin{aligned}g_b^{n-1} = &\left[\mu \frac{\mathrm{cov}\left(\hat{M}_b^{\mathrm{LR}}, P^{\mathrm{HR}}\right)}{\mathrm{var}\left(P^{\mathrm{HR}}\right)} + (1-\mu) \frac{\mathrm{cov}\left(\hat{M}_b^{\mathrm{LR}}, P^{\mathrm{LR}}\right)}{\mathrm{var}\left(P^{\mathrm{HR}}\right)}\right] \\ &\cdot \sum_{i=0}^{n-1} \left[1 - \frac{\mathrm{cov}\left(P^{\mathrm{HR}}, P^{\mathrm{LR}}\right)}{\mathrm{var}\left(P^{\mathrm{HR}}\right)}\right]^i.\end{aligned} \tag{29}$$

Finally, to show that the dual-scale regression model is iterative and convergent, mathematical induction is used to obtain g_b^n derived from g_b^{n-1} in (30) as

$$\begin{aligned}g_b^{n} = &\left[\mu \frac{\mathrm{cov}\left(\hat{M}_b^{\mathrm{LR}}, P^{\mathrm{HR}}\right)}{\mathrm{var}\left(P^{\mathrm{HR}}\right)} + (1-\mu) \frac{\mathrm{cov}\left(\hat{M}_b^{\mathrm{LR}}, P^{\mathrm{LR}}\right)}{\mathrm{var}\left(P^{\mathrm{HR}}\right)}\right] \\ &\cdot \sum_{i=0}^{n} \left[1 - \frac{\mathrm{cov}\left(P^{\mathrm{HR}}, P^{\mathrm{LR}}\right)}{\mathrm{var}\left(P^{\mathrm{HR}}\right)}\right]^i.\end{aligned} \tag{30}$$

Similarly, the iterative process used in the regression requires a fixed point when n approaches infinity. Therefore, g_b^∞ is defined as follows:

$$\begin{aligned}g_b^{\infty} &= \lim_{n\to\infty} g_b^n \\ &= \left[\mu \frac{\mathrm{cov}\left(\hat{M}_b^{\mathrm{LR}}, P^{\mathrm{HR}}\right)}{\mathrm{var}\left(P^{\mathrm{HR}}\right)} + (1-\mu) \frac{\mathrm{cov}\left(\hat{M}_b^{\mathrm{LR}}, P^{\mathrm{LR}}\right)}{\mathrm{var}\left(P^{\mathrm{HR}}\right)}\right] \\ &\quad\cdot \sum_{i=0}^{\infty} \left[1 - \frac{\mathrm{cov}\left(P^{\mathrm{HR}}, P^{\mathrm{LR}}\right)}{\mathrm{var}\left(P^{\mathrm{HR}}\right)}\right]^i.\end{aligned} \tag{31}$$

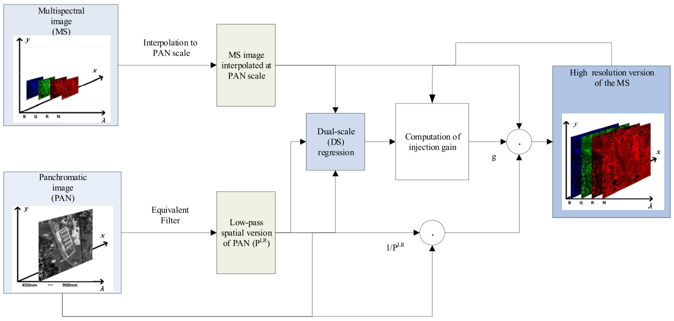

Fig. 1. Flowchart of MTF-GLP-HPM-DS.

Particularly, due to the fact that

$$0 < \left| 1 - \frac{\mathrm{cov}\left(P^{\mathrm{HR}}, P^{\mathrm{LR}}\right)}{\mathrm{var}\left(P^{\mathrm{HR}}\right)} \right| < 1. \tag{32}$$

We have

$$g_b^{\infty} = \mu \frac{\mathrm{cov}\left(\hat{M}_b^{\mathrm{LR}}, P^{\mathrm{HR}}\right)}{\mathrm{cov}\left(P^{\mathrm{HR}}, P^{\mathrm{LR}}\right)} + (1-\mu)\frac{\mathrm{cov}\left(\hat{M}_b^{\mathrm{LR}}, P^{\mathrm{LR}}\right)}{\mathrm{cov}\left(P^{\mathrm{HR}}, P^{\mathrm{LR}}\right)}. \tag{33}$$

As presented in (33), g_b^{∞} has a fixed value. Based on (28)–(33), the proposed dual-scale regression model is iterative and convergent. When g_b reaches this fixed value, it is assumed that the convergence is achieved, and the iterative operations are stopped.

The process of the proposed MTF-GLP-HPM-DS is presented in Algorithm 2. The injection coefficients g_b are obtained after each iteration and substituted into (26) to obtain the pansharpening result. When the iterative process is stopped, the final pansharpening result is obtained. Fig. 1 shows the flowchart of MTF-GLP-HPM-DS pansharpening method.

Algorithm 2: Proposed MTF-GLP-HPM-DS

Input: an LR-MS image and an HR-PAN image

1) Interpolate the LR-MS image to the size of the HR-PAN image;
2) Obtain P^{LR} using the HR-PAN image using the MTF-GLP;
3) Calculate the gain coefficients g_b using (27);

for $i = 0, \ldots, N-1$ **do**

- Calculate the injection coefficients g_b^i as:

$$g_b^i = \mu \frac{\mathrm{cov}\left(M_b^{\mathrm{HR},i}, P^{\mathrm{HR}}\right)}{\mathrm{cov}\left(P^{\mathrm{LR}}, P^{\mathrm{HR}}\right)} + (1-\mu)\frac{\mathrm{cov}\left(M_b^{\mathrm{HR},i}, P^{\mathrm{LR}}\right)}{\mathrm{cov}\left(P^{\mathrm{LR}}, P^{\mathrm{HR}}\right)}$$

- Use g_b^i to fuse the MS and PAN as follows:

$$M_b^{\mathrm{HR},i+1} = \hat{M}_b^{\mathrm{LR}} \frac{P^{\mathrm{HR}} - \mathrm{E}\left(P^{\mathrm{HR}}\right) + \mathrm{E}\left(M_b^{\mathrm{HR}}\right)/g_b^i}{P^{\mathrm{LR}} - \mathrm{E}\left(P^{\mathrm{HR}}\right) + \mathrm{E}\left(M_b^{\mathrm{HR}}\right)/g_b^i}$$

end

4) Stop the iterative process;

Output: M_b^{HR}

III. Experiments

A. Experimental Design

There are two types of quality assessments used to evaluate pansharpening, namely, reduced resolution and full resolution. Please note that the pansharpening results should satisfy two metrics, including consistency and synthesis [2]. The consistency shows that the pansharpening result once degraded at the original MS resolution, should be spectrally similar to the original MS image as much as possible. The synthesis requires the pansharpening result to be similar to the image obtained by the MS sensor. Meanwhile, the reduced resolution evaluation is to reduce the resolution on the basis of the original MS image, so that the original MS image can be used as the reference image of the pansharpening result as they have the same size.

Reduced resolution assessment: We evaluate the synthesis property of Wald's protocol [46], [47], and the following quality/distortion quantitative indices are used for performance evaluation.

The relative dimensionless global error in synthesis (ERGAS) [48] denotes a normalized dissimilarity index. It represents a global indicator of the multi-band distortion of the pansharpening results. Generally, a low ERGAS value indicates a high similarity between the pansharpening result and the reference MS image.

The SAM [49] represents an absolute value of the spectral angle between two-pixel vectors. When the pansharpening result is spectrally identical to the reference image, SAM is assumed to be ideal, i.e., zero.

Another (scalar) index of the pansharpening result with 2^n bands is called Q-index, denoted as $\mathrm{Q}2^{\mathrm{n}}$ [50]. $\mathrm{Q}2^n$ ranges between [0, 1], and its ideal value is 1.

Full-resolution assessment: The quality no-reference (QNR) protocol is used to perform the quality evaluation for the original resolution of the data [51] as follows:

$$\mathrm{QNR} = (1 - D_\lambda)^{\varepsilon}(1 - D_S)^{\theta} \tag{34}$$

where, $Q(A, B)$ denotes the Q-index between A and B; D_λ denotes the spectral distortion, which is calculated using the original LR-MS image and the pansharpening result; D_S represents the spatial distortion, which combines the Q-index between the original LR-MS image and the LR-PAN image and the Q-index between the pansharpening result and the HR-PAN image. The parameter p is typically set to 1. ε and θ represent the weight coefficients. It is notable that higher the QNR index, lower is the D_λ index. A lower D_S index indicates a better quality of pansharpening result. Therefore, the maximum theoretical value of the QNR index is 1, when both D_λ and D_S are equal to zero.

The performance of the proposed MTF-GLP-HPM-DS is compared with the state-of-the-art methods for MRA including.

1) *EXP:* The MS image interpolation using a polynomial kernel with 23 coefficients [2].
2) *BT-H:* The haze corrected version of the Brovey transform [38].
3) *C-GSA:* Context-adaptive Gram-Schmidt [35].

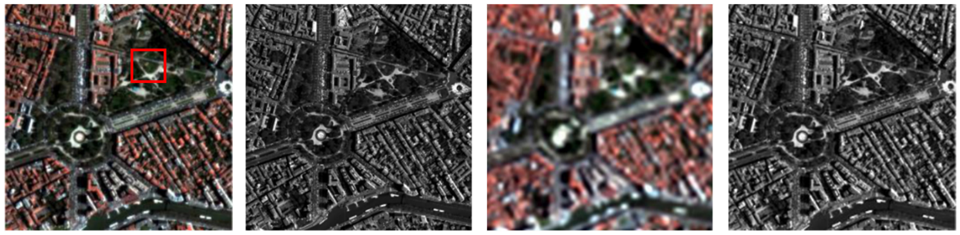

(a) (b) (c) (d)

Fig. 2. Toulouse dataset. (a) Original MS image. (b) Original PAN image. (c) Reduced resolution MS image. (d) Reduced resolution PAN image.

TABLE I
PARAMETERS OF FIVE DATASETS

Dataset			Spatial resolution	Spectral dimension	Dimension size	Thematic scene	The parameter μ
Reduced resolution	Toulouse dataset	PAN	0.15m	1 band	1024 × 1024	Buildings	0.05
		MS	0.6m	4 bands	256 × 256×4		
	WorldView-3 sensor dataset	PAN	0.31m	1 band	1024 × 1024	Vegetation	0.95
		MS	1.24m	8 bands	256 × 256×8		
	IKONOS sensor dataset	PAN	1m	1 band	1024 × 1024	Water	0.5
		MS	4m	4 bands	256 × 256×4		
Full resolution	QuickBird sensor dataset	PAN	0.61m	1 band	1024 × 1024	Water	0.05
		MS	2.44m	4 bands	256 × 256×4		
	WorldView-2 sensor dataset	PAN	0.5m	1 band	1024 × 1024	Buildings	0.05
		MS	2m	8 bands	256 × 256×8		

4) AWLP with revised statistical matching between PAN and MS bands [30].
5) *MTF-GLP:* GLP with MTF-matched filter, unitary injection model, and revised statistical matching between the PAN and MS bands [33].
6) *MTF-GLP-REG-FS:* GLP with MTF-matched filter with a full-scale regression-based injection model [41].
7) *MTF-GLP-CBD:* GLP with MTF-matched filter and regression-based injection model [34].
8) *C-MTF-GLP-CBD:* The context-based GLP with MTF-matched filter and regression-based injection model with local parameter estimation that exploits clustering [34], [35].
9) *MF:* A nonlinear decomposition scheme using MFs based on half gradient [32].
10) *MTF-GLP-HPM:* GLP with MTF-matched filter with HPM injection model and revised statistical matching between the PAN and MS bands [36].
11) *MTF-GLP-HPM-H:* GLP with MTF-matched filter with HPM injection model and haze correction [38].
12) *MTF-GLP-HPM-R:* GLP with MTF-matched filter and HPM injection model with a preliminary regression-based spectral matching phase [42].
13) *MTF-GLP-HPM-PP:* GLP with MTF-matched filter, multiplicative injection model and post-processing [39].

Please note that all the compared methods use the pansharpening toolbox available at http://openremotesensing.net/knowledgebase/a-new-benchmark-based-on-recent-advances-in-multispectral-pansharpening-revisiting-pansharpening-with-classical-and-emerging-pansharpening-methods/.

In addition, to highlight the performance of the proposed dual-scale regression, an MRA based on the scale regression model and improved using the HPM injection scheme described in Sections II-A and II-B, namely MTF-GLP-HPM-FS, is used as an additional comparative method for evaluating the proposed MTF-GLP-HPM-DS. All the experiments presented in this work are performed on a Pentium (R) Dual-core Processor (2.20 GHz) using MATLAB R2016 software.

B. Reduced Resolution

As presented in Table I, we use three datasets obtained by different sensors for evaluating the reduced resolution [52]. In the reduced resolution experiments, the reduced resolution input MS image and the reduced resolution input PAN image are obtained by performing low-pass filtering at a spatial resolution ratio of $R = 4$.

1) Toulouse Dataset: This dataset comprises images of buildings in an urban area of Toulouse (France), which are acquired by an aerial CNES platform. As shown in Fig. 2(a), the original MS images have a size of 256 × 256 pixels, and have four spectral bands, and a spatial resolution of 0.6 m. We use these as the reference images. The original PAN images are presented in Fig. 2(b). The size of each PAN image is 1024 × 1024 pixels with a spatial resolution of 0.15 m. As shown in Fig. 2(c) and (d), the reduced resolution MS image with a size of 64 × 64 pixels and reduced resolution PAN image with a size of 256 × 256 pixels are obtained by down-sampling the original MS and PAN images using a low-pass filter with a spatial resolution ratio of $R = 4$. Therefore, the derived pansharpening result has a size of 256×256 pixels and can be compared with the reference image. In this dataset, $\mu = 0.05$.

2) WorldView-3 Sensor Dataset: This dataset comprises imagery of green vegetation in the rural area. The original MS images have a size of 256 × 256 pixels, and have eight spectral bands, and a spatial resolution of 1.24 m. These are used as reference images. The original PAN images have a

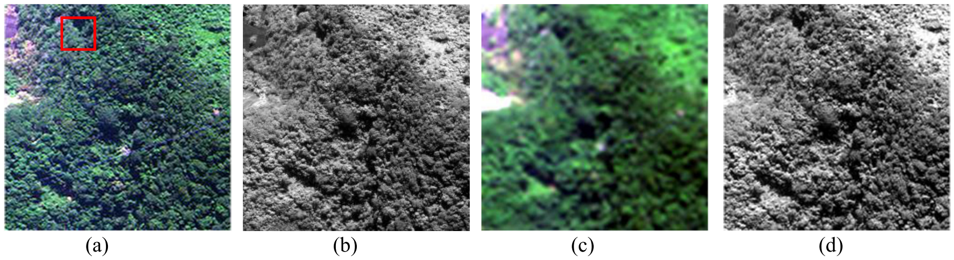

Fig. 3. WorldView-3 sensor dataset. (a) Original MS image. (b) Original PAN image. (c) Reduced resolution MS image. (d) Reduced resolution PAN image.

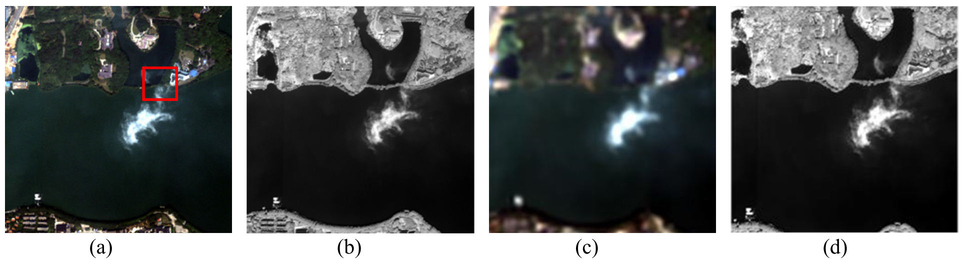

Fig. 4. IKONOS sensor dataset. (a) Original MS image. (b) Original PAN image. (c) Reduced resolution MS image. (d) Reduced resolution PAN image.

TABLE II
ASSESSMENT FOR THE TOULOUSE DATASET OF FIFTEEN METHODS AT REDUCED RESOLUTION

	Q4	SAM	ERGAS
Reference	1.0000	0.0000	0.0000
EXP	0.6421	4.6256	5.8316
BT-H	0.8725	5.3534	4.9744
C_GSA	0.8728	7.3863	4.7470
AWLP	0.8752	5.9812	4.9724
MTF-GLP	0.8666	4.8369	5.0168
MTF-GLP-FS	0.8917	5.1124	4.1392
MTF-GLP-CBD	0.8901	5.3889	4.2031
C-MTF-GLP-CBD	0.8872	6.9655	4.4196
MF	0.8905	**4.2028**	3.8949
MTF-GLP-HPM	0.8722	4.2719	4.8736
MTF-GLP-HPM-R	0.8913	5.5609	4.2094
MTF-GLP-HPM-H	0.8709	5.6762	5.1628
MTF-GLP-HPM-PP	0.8634	4.9163	4.2391
MTF-GLP-HPM-FS	0.8913	5.5609	4.2094
MTF-GLP-HPM-DS	**0.9016**	5.1068	**3.8083**

size of 1024×1024 pixels and a spatial resolution of 0.31 m. The spatial resolution ratio of $R = 4$ is used to produce the reduced resolution MS and PAN images. The instances of the WorldView-3 sensor dataset are shown in Fig. 3. The parameter μ for this dataset is 0.95.

3) IKONOS Sensor Dataset: This dataset comprises the images of water in suburban area. The original MS images have a size of 256×256 pixels, and have four spectral bands, and a spectral resolution of 4 m. These images are used as the reference images. The original PAN image has a size of 1024×1024 pixels and has a spatial resolution of 1 m. Similarly, the reduced resolution MS and PAN images are obtained using the spatial resolution ratio of $R = 4$. The instances of the IKONOS sensor dataset are presented in Fig. 4. The parameter μ for this dataset is 0.5.

To show the differences of pansharpened images better in reduced resolution experiments, the SAM error maps of the sub-areas which are framed in Figs. 2(a), 3(a), and 4(a). The pansharpening results of the Toulouse dataset at reduced resolution are shown in Fig. 5 and the SAM error maps are shown in Fig. 6. It is evident that MTF-GLP-HPM-DS in Fig. 5(o) is most similar to the reference image presented in Fig. 2(a). There is the least error in Fig. 6(o). Three evaluation indices at reduced resolution are presented in Table II, where it can be seen that $Q2^n$ is equal to $Q4$ due to four spectral bands in the Toulouse sensor dataset. The three evaluation indices demonstrate that the proposed MTF-GLP-HPM-DS has a better performance in terms of Wald's protocol as compared to the other methods. Although the SAM of MTF-GLP-HPM-DS is not better than the best result, the values of $Q4$ of the proposed method are closest to 1 as compared to the other methods, while its ERGAS value is the lowest.

The WorldView-3 dataset is used to illustrate the performance of the proposed method on MS images with eight spectral bands. In this test, $Q2^n$ is equal to $Q8$. The visual performance and quality assessment of 15 pansharpening results for the WorldView-3 sensor dataset at a reduced resolution are shown in Fig. 7, the SAM error maps in Fig. 8 and Table III. The results show that the proposed MTF-GLP-HPM-DS achieves the best performance in terms of both the visual and index comparison.

The visual comparison and quality assessment of 15 pansharpening results obtained using the IKONOS sensor dataset at a reduced resolution are shown in Fig. 9, the SAM error maps in Fig. 10 and Table IV. The results in Table IV show that the proposed MTF-GLP-HPM-DS method obtains the highest value in for $Q4$ and lowest value for SAM among all the compared methods. Although the value of ERGAS for the MTF-GLP-HPM-DS method is not the lowest, it is very close to the best-obtained value of the MF method. This was because a lower μ value brought a better Q-index and SAM value but a worse ERGAS, so μ of 0.5 was used to balance the performance. In general, the proposed method achieves the best performance among all the compared methods.

C. Full Resolution

We evaluate two datasets under a full resolution [53], [54] as shown in Table I.

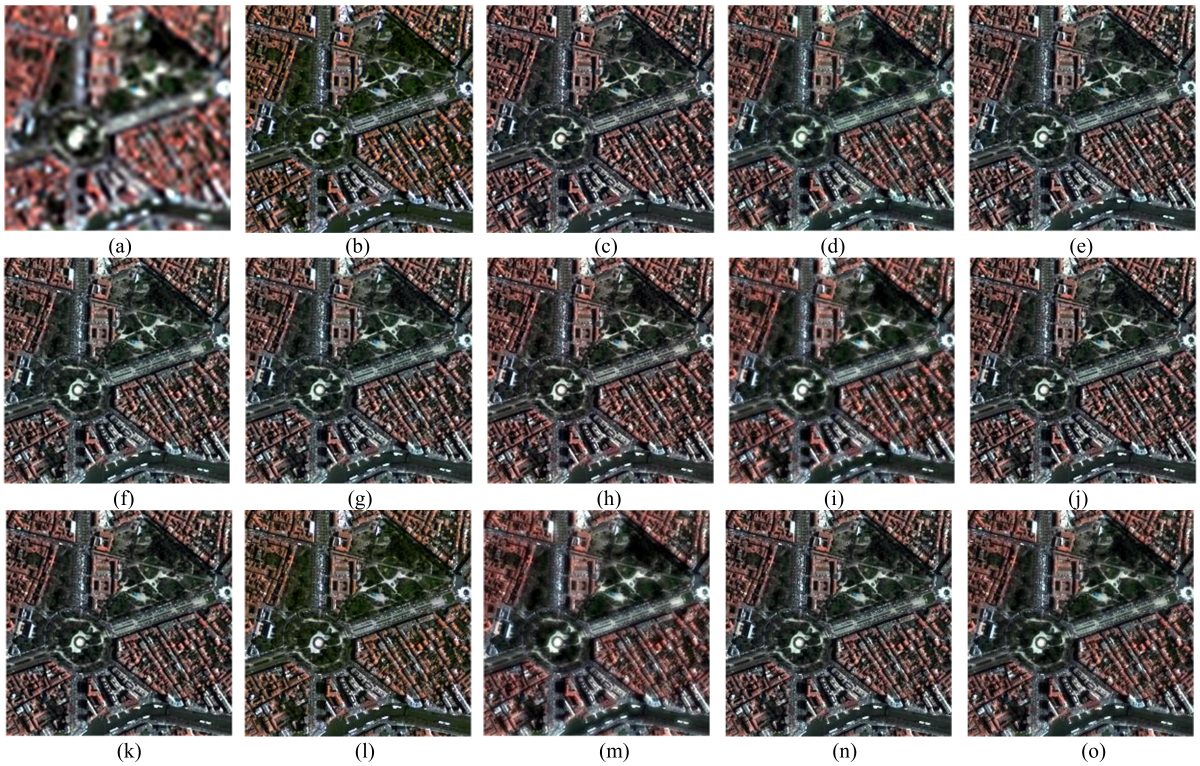

Fig. 5. Results of Toulouse dataset at reduced resolution. (a) EXP. (b) BT-H. (c) C-GSA. (d) AWLP. (e) MTF-GLP. (f) MTF-GLP-FS. (g) MTF-GLP-CBD. (h) C-MTF-GLP-CBD. (i) MF. (j) MTF-GLP-HPM. (k). MTF-GLP-HPM-R. (l) MTF-GLP-HPM-H. (m) MTF-GLP-HPM-PP. (n) MTF-GLP-HPM-FS. (o) MTF-GLP-HPM-DS.

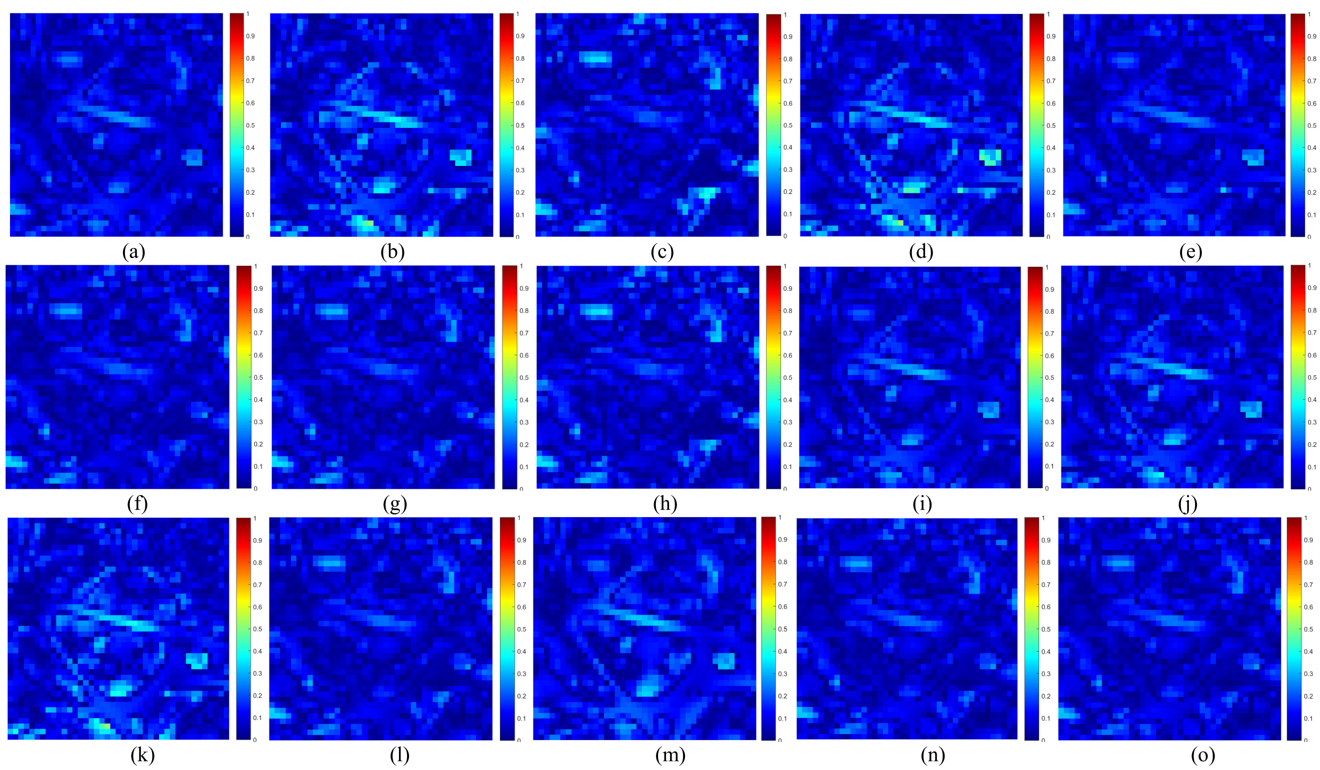

Fig. 6. Subareas of SAM maps for Toulouse dataset at reduced resolution. (a) EXP. (b) BT-H. (c) C-GSA. (d) AWLP. (e) MTF-GLP. (f) MTF-GLP-FS. (g) MTF-GLP-CBD. (h) C-MTF-GLP-CBD. (i) MF. (j) MTF-GLP-HPM. (k). MTF-GLP-HPM-R. (l) MTF-GLP-HPM-H. (m) MTF-GLP-HPM-PP. (n) MTF-GLP-HPM-FS. (o) MTF-GLP-HPM-DS.

1) QuickBird Sensor Dataset: This dataset is acquired under the water in a suburban area. In the full-resolution assessment, the original MS images have a size of 256 $\times$ 256 pixels, have four spectral bands, and a spectral resolution of 2.44 m, as shown in Fig. 11(a). The original PAN images have a size of 1024 $\times$ 1024 pixels and a spatial resolution of 0.61 m,

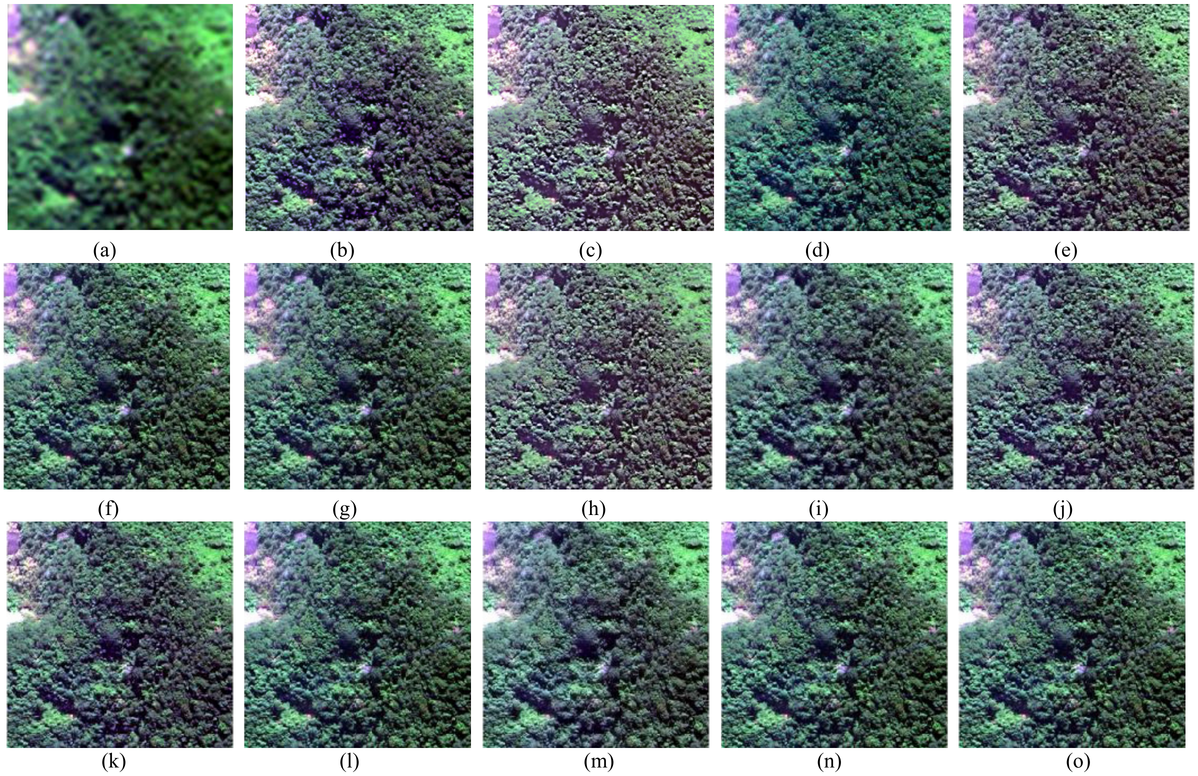

Fig. 7. Results of WorldView-3 dataset at reduced resolution. (a) EXP. (b) BT-H. (c) C-GSA. (d) AWLP. (e) MTF-GLP. (f) MTF-GLP-FS. (g) MTF-GLP-CBD. (h) C-MTF-GLP-CBD. (i) MF. (j) MTF-GLP-HPM. (k). MTF-GLP-HPM-R. (l) MTF-GLP-HPM-H. (m) MTF-GLP-HPM-PP. (n) MTF-GLP-HPM-FS. (o) MTF-GLP-HPM-DS.

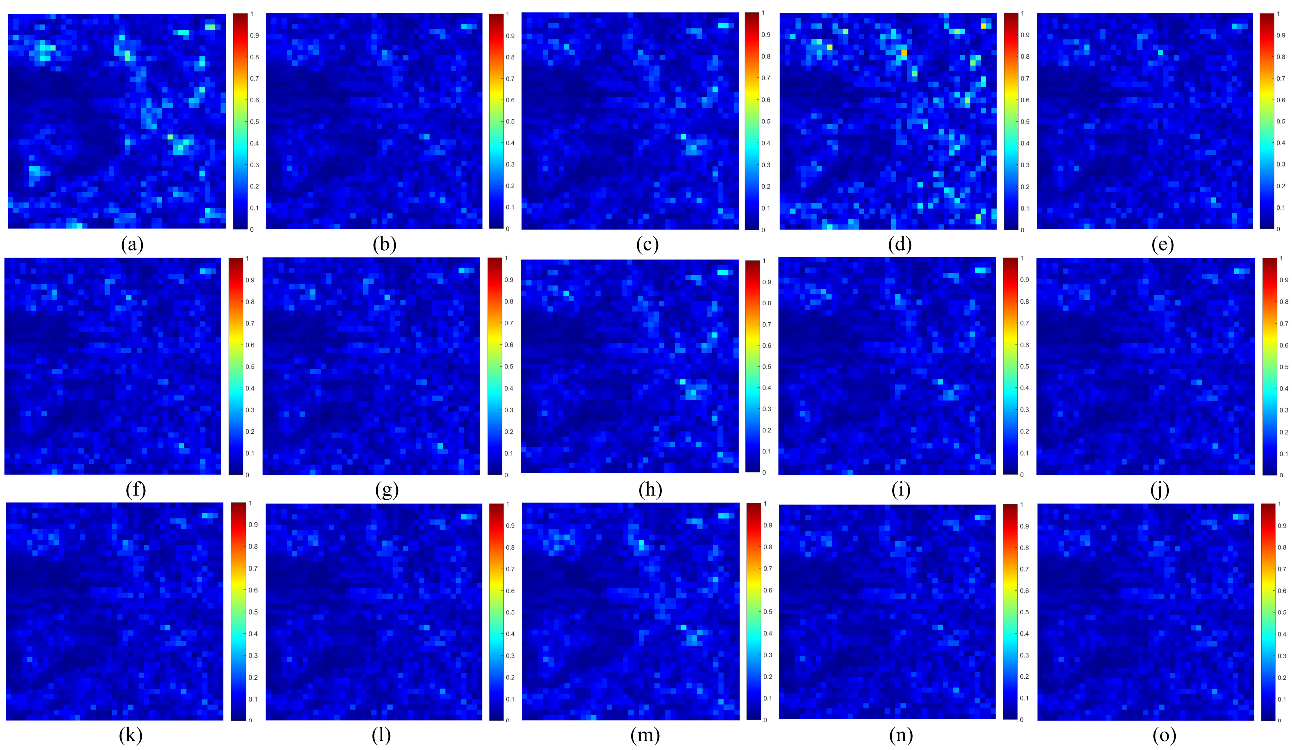

Fig. 8. Subareas of SAM maps for WorldView-3 dataset at reduced resolution. (a) EXP. (b) BT-H. (c) C-GSA. (d) AWLP. (e) MTF-GLP. (f) MTF-GLP-FS. (g) MTF-GLP-CBD. (h) C-MTF-GLP-CBD. (i) MF. (j) MTF-GLP-HPM. (k). MTF-GLP-HPM-R. (l) MTF-GLP-HPM-H. (m) MTF-GLP-HPM-PP. (n) MTF-GLP-HPM-FS. (o) MTF-GLP-HPM-DS.

as shown in Fig. 11(b). These images are directly used as the input data. Therefore, the derived pansharpening result has a size of 1024×1024 pixels. Here, the parameter μ is 0.05.

2) WorldView-2 Sensor Dataset: This dataset comprises the images of buildings in an urban area. The original MS image with a size of 256×256 pixels, eight spectral bands spectral,

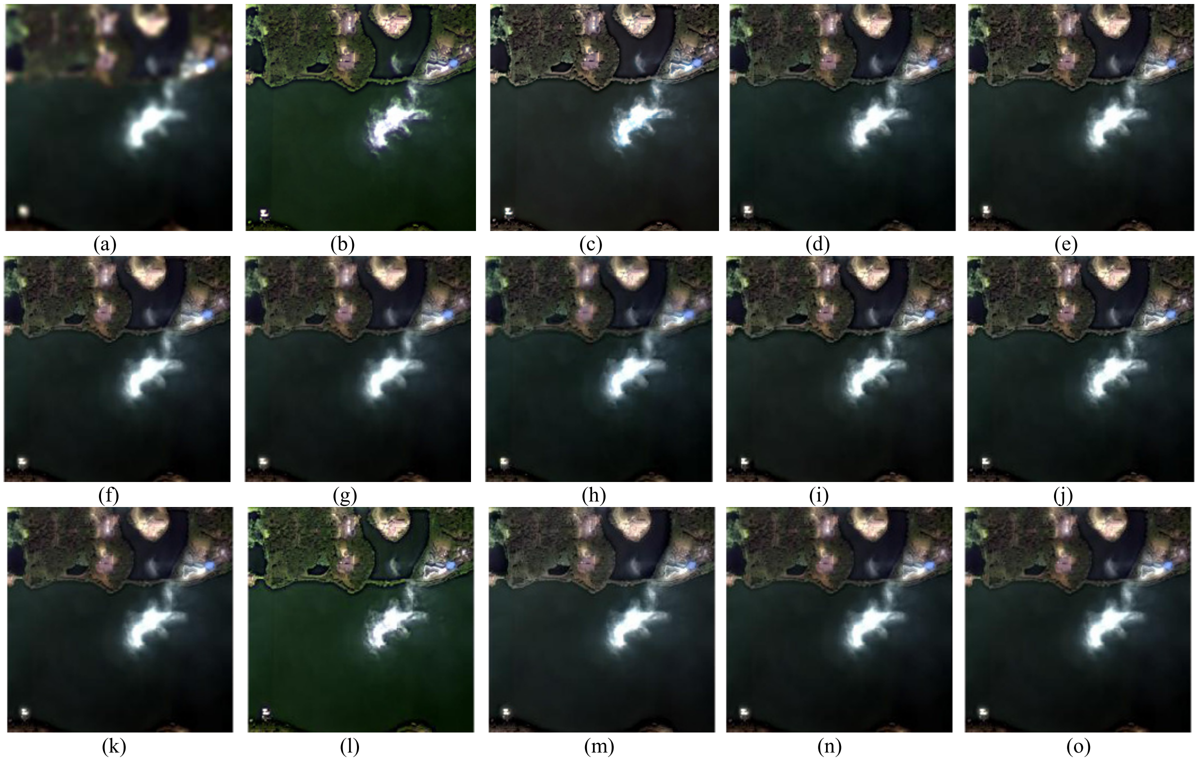

Fig. 9. Results of IKONOS sensor dataset at reduced resolution. (a) EXP. (b) BT-H. (c) C-GSA. (d) AWLP. (e) MTF-GLP. (f) MTF-GLP-FS. (g) MTF-GLP-CBD. (h) C-MTF-GLP-CBD. (i) MF. (j) MTF-GLP-HPM. (k). MTF-GLP-HPM-R. (l) MTF-GLP-HPM-H. (m) MTF-GLP-HPM-PP. (n) MTF-GLP-HPM-FS. (o) MTF-GLP-HPM-DS.

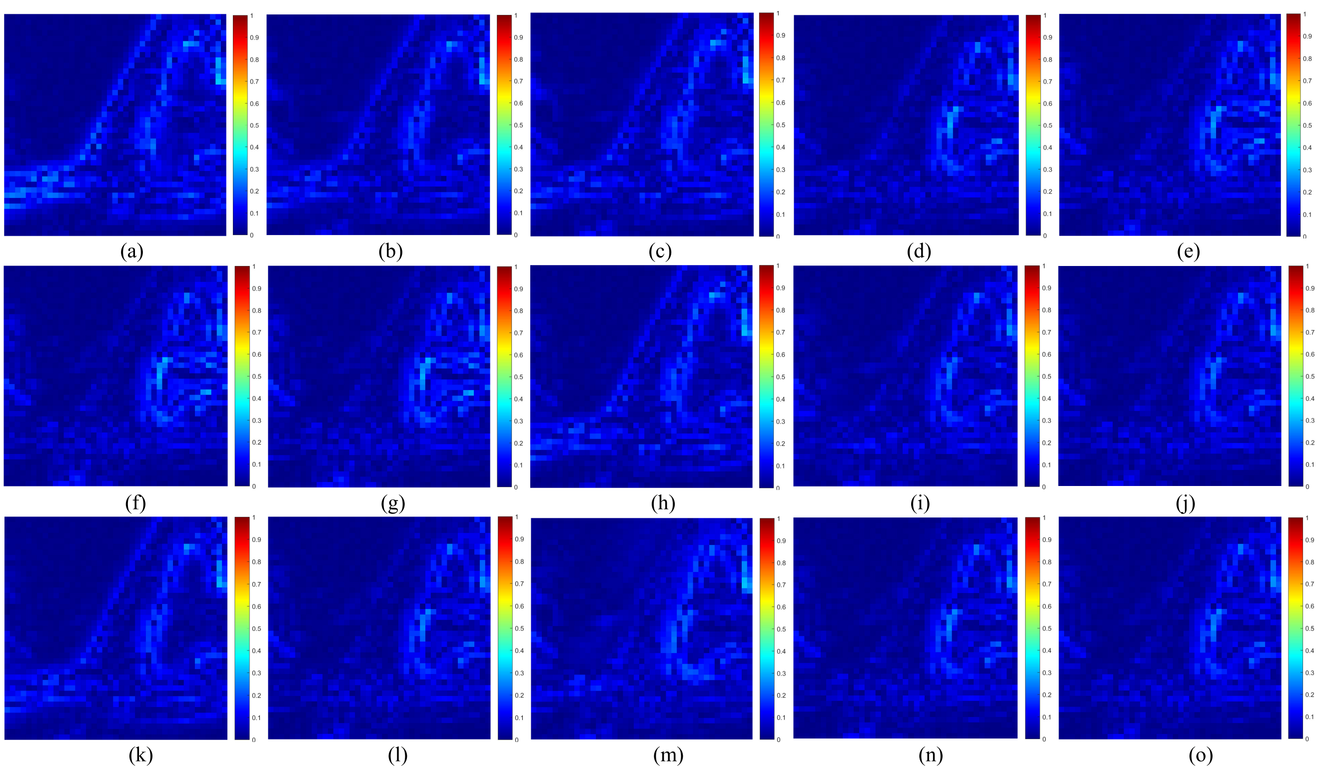

Fig. 10. Subareas of SAM maps for IKONOS sensor dataset at reduced resolution. (a) EXP. (b) BT-H. (c) C-GSA. (d) AWLP. (e) MTF-GLP. (f) MTF-GLP-FS. (g) MTF-GLP-CBD. (h) C-MTF-GLP-CBD. (i) MF. (j) MTF-GLP-HPM. (k). MTF-GLP-HPM-R. (l) MTF-GLP-HPM-H. (m) MTF-GLP-HPM-PP. (n) MTF-GLP-HPM-FS. (o) MTF-GLP-HPM-DS.

and a spectral resolution of 2 m is presented in Fig. 12(a). The original PAN image with a size of 1024×1024 pixels and a spatial resolution of 0.5 m is displayed in Fig. 12(b). For this dataset, $\mu = 0.05$.

TABLE III

ASSESSMENT FOR THE WORLDVIEW-3 SENSOR DATASET OF 15 METHODS AT REDUCED RESOLUTION

	Q8	SAM	ERGAS
Reference	1.0000	0.0000	0.0000
EXP	0.4346	9.1372	5.7648
BT-H	0.8215	6.3310	3.6132
C_GSA	0.7834	7.7104	4.1460
AWLP	0.8251	8.9408	4.2858
MTF-GLP	0.8205	6.3226	3.6700
MTF-GLP-FS	0.8266	6.3006	3.5550
MTF-GLP-CBD	0.8267	6.3177	3.5585
C-MTF-GLP-CBD	0.7941	7.7165	4.1149
MF	0.8209	6.8949	3.8207
MTF-GLP-HPM	0.8222	6.2525	3.6476
MTF-GLP-HPM-R	0.8262	6.2455	3.5634
MTF-GLP-HPM-H	0.8270	6.2773	3.5388
MTF-GLP-HPM-PP	0.8071	7.3480	3.9863
MTF-GLP-HPM-FS	0.8269	6.2537	3.5357
MTF-GLP-HPM-DS	**0.8285**	**6.2149**	**3.5323**

TABLE IV

ASSESSMENT FOR THE IKONOS SENSOR DATASET OF 15 METHODS AT REDUCED RESOLUTION

	Q4	SAM	ERGAS
Reference	1.0000	0.0000	0.0000
EXP	0.7400	1.7864	2.9634
BT-H	0.7391	1.5033	1.9276
C_GSA	0.7157	1.6235	2.1007
AWLP	0.7775	1.2874	1.8652
MTF-GLP	0.7659	1.3770	1.8982
MTF-GLP-FS	0.7801	1.3451	1.8851
MTF-GLP-CBD	0.7801	1.3445	1.8874
C-MTF-GLP-CBD	0.7767	1.3164	1.7627
MF	0.7621	1.3308	1.8429
MTF-GLP-HPM	0.7755	1.2320	**1.6734**
MTF-GLP-HPM-R	0.7866	1.2207	1.6753
MTF-GLP-HPM-H	0.7733	1.4446	1.7632
MTF-GLP-HPM-PP	0.7318	1.4896	2.0043
MTF-GLP-HPM-FS	0.7866	1.2206	1.6741
MTF-GLP-HPM-DS	**0.7869**	**1.2203**	1.6742

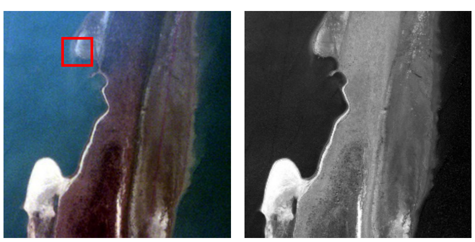

(a) (b)

Fig. 11. QuickBird sensor dataset. (a) original MS image. (b) original PAN image.

(a) (b)

Fig. 12. WorldView-2 sensor dataset. (a) original MS image. (b) original PAN image.

Because there are no reference images in full resolution experiments, the subareas which are framed in Figs. 11(a) and 12(a) are magnified in Figs. 14 and 16.

TABLE V

ASSESSMENT FOR THE QUICKBIRD SENSOR DATASET OF 15 METHODS AT FULL RESOLUTION

	D_λ	D_S	QNR
Reference	0.0000	0.0000	1.0000
EXP	0.0000	0.1447	0.8553
BT-H	0.1478	0.2410	0.6468
C_GSA	0.1787	0.2472	0.6183
AWLP	0.1303	0.1661	0.7252
MTF-GLP	0.0987	0.1545	0.7620
MTF-GLP-FS	0.0410	0.0906	0.8720
MTF-GLP-CBD	0.0409	0.0903	0.8725
C-MTF-GLP-CBD	0.2325	0.2467	0.5781
MF	0.1129	0.1557	0.7490
MTF-GLP-HPM	0.0998	0.1548	0.7608
MTF-GLP-HPM-R	0.1459	0.2122	0.6729
MTF-GLP-HPM-H	0.0412	0.0899	0.8726
MTF-GLP-HPM-PP	0.1467	0.1800	0.6997
MTF-GLP-HPM-FS	0.0413	0.0903	0.8721
MTF-GLP-HPM-DS	**0.0409**	**0.0898**	**0.8728**

TABLE VI

ASSESSMENT FOR THE WORLDVIEW-2 SENSOR DATASET OF 15 METHODS AT FULL RESOLUTION

	D_λ	D_S	QNR
Reference	0.0000	0.0000	1.0000
EXP	0.0000	0.0598	0.9402
BT-H	0.0642	0.0752	0.8654
C_GSA	0.0537	0.0719	0.8783
AWLP	0.0673	0.0504	0.8857
MTF-GLP	0.0879	0.0687	0.8495
MTF-GLP-FS	0.0592	0.0577	0.8865
MTF-GLP-CBD	0.0578	0.0570	0.8885
C-MTF-GLP-CBD	0.0513	0.0502	0.9010
MF	0.0904	0.0644	0.8510
MTF-GLP-HPM	0.0745	0.0659	0.8645
MTF-GLP-HPM-R	0.0456	0.0482	0.9084
MTF-GLP-HPM-H	0.0858	0.0692	0.8509
MTF-GLP-HPM-PP	0.1132	0.0847	0.8117
MTF-GLP-HPM-FS	0.0464	0.0486	0.9072
MTF-GLP-HPM-DS	**0.0449**	**0.0480**	**0.9093**

The visual results and evaluation indicators of the QuickBird dataset obtained using the 15 pansharpening methods at a full resolution are presented in Fig. 13, the subareas in Fig. 14 and Table V. The experimental results show that the proposed MTF-GLP-HPM-DS achieves the best performance among all the compared methods. The MTF-GLP-HPM-DS method has the smallest D_λ and D_S, and the QNR is very close to 1.

The pansharpening results and evaluation indicators for the WorldView-2 dataset [55] are shown in Fig. 15, the subareas in Fig. 16 and Table VI. Similar to the results obtained using the QuickBird sensor dataset at a full resolution, the proposed MTF-GLP-HPM-DS obtains the lowest values for D_λ and D_S and the highest QNR value among all the compared methods. These results confirm that the proposed method has a good capability to process the urban scenario images. Based on the overall results, the proposed MTF-GLP-HPM-DS is always superior to the other state-of-the-art methods in terms of both the reduced resolution assessment and the full-resolution assessment.

IV. DISCUSSION

A. Spatial Resolution Ratio R

The different values of R indicate that the reduced resolution MS with a different resolution is obtained. Therefore, this

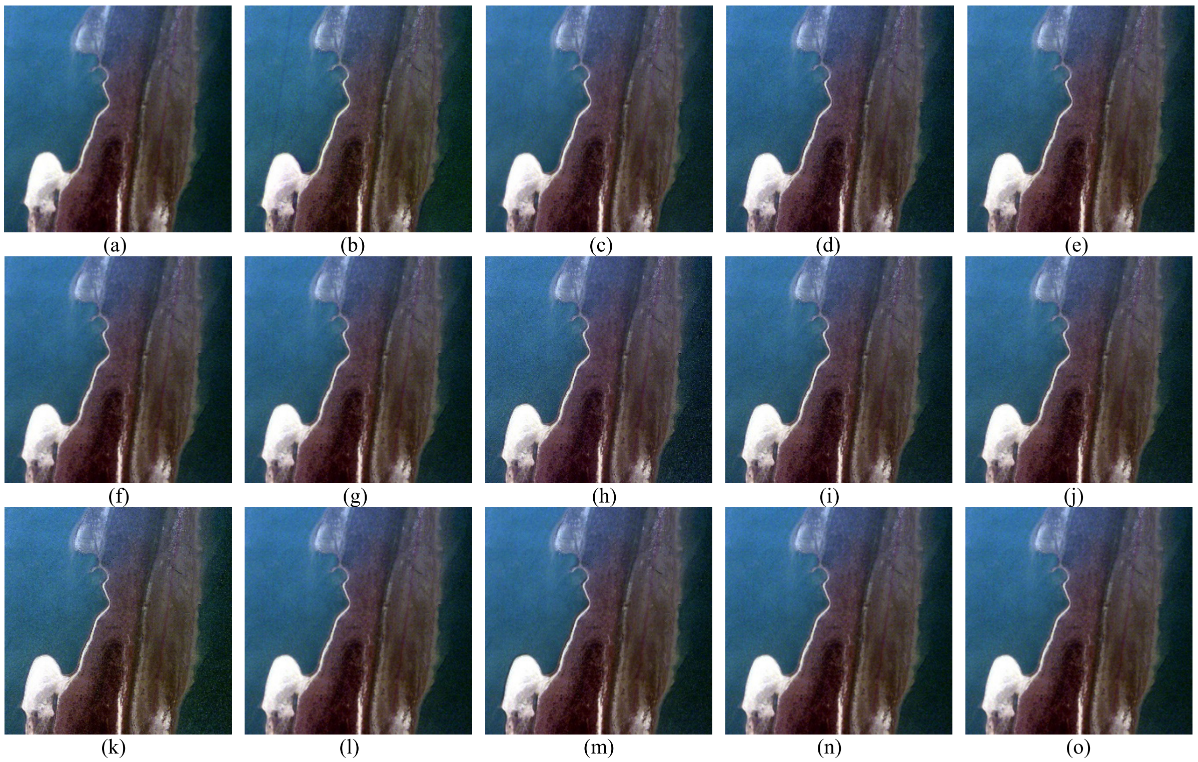

Fig. 13. Results of QuickBird sensor dataset at full resolution. (a) EXP. (b) BT-H. (c) C-GSA. (d) AWLP. (e) MTF-GLP. (f) MTF-GLP-FS. (g) MTF-GLP-CBD. (h) C-MTF-GLP-CBD. (i) MF. (j) MTF-GLP-HPM. (k). MTF-GLP-HPM-R. (l) MTF-GLP-HPM-H. (m) MTF-GLP-HPM-PP. (n) MTF-GLP-HPM-FS. (o) MTF-GLP-HPM-DS.

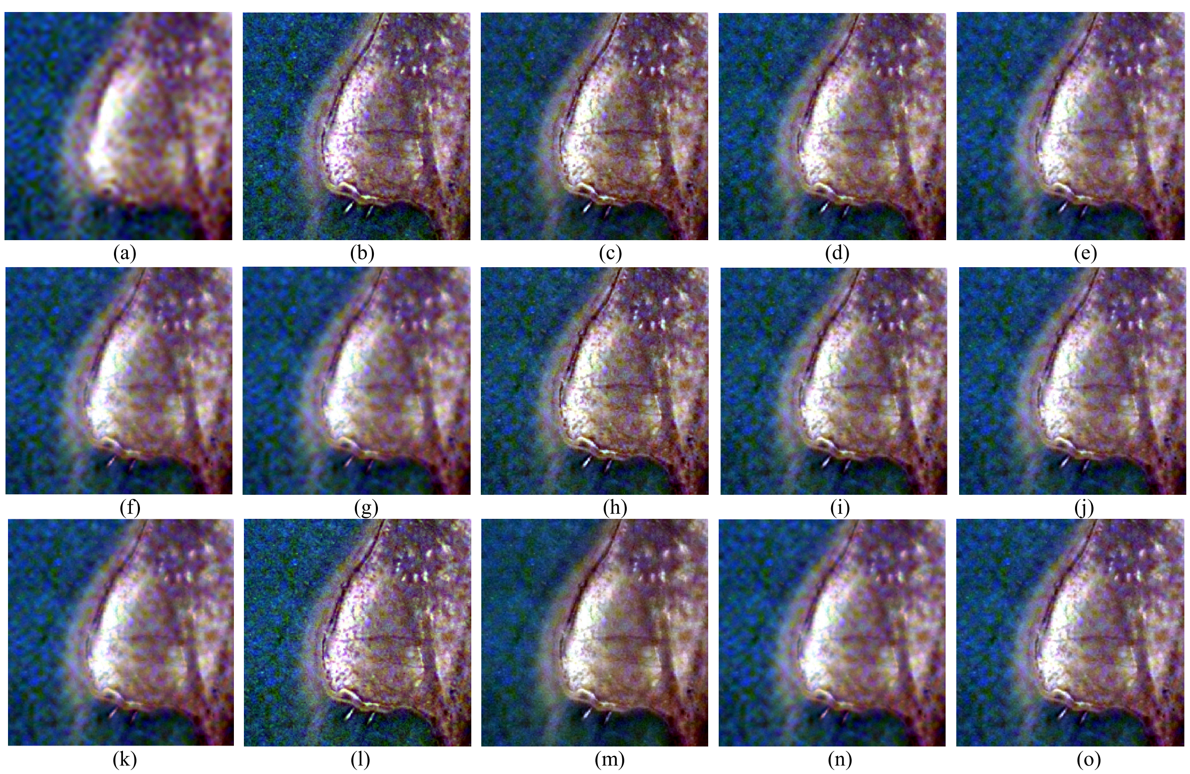

Fig. 14. Subareas of QuickBird sensor dataset at full resolution. (a) EXP. (b) BT-H. (c) C-GSA. (d) AWLP. (e) MTF-GLP. (f) MTF-GLP-FS. (g) MTF-GLP-CBD. (h) C-MTF-GLP-CBD. (i) MF. (j) MTF-GLP-HPM. (k). MTF-GLP-HPM-R. (l) MTF-GLP-HPM-H. (m) MTF-GLP-HPM-PP. (n) MTF-GLP-HPM-FS. (o) MTF-GLP-HPM-DS.

experiment evaluates the performance of the proposed MTF-GLP-HPM-DS method for another spatial resolution ratio, i.e., $R = 2$, for MS on the Toulouse and IKONOS datasets. In this experiment, the reduced resolution PAN image is again obtained by down-sampling the original PAN image using a low-pass filter with a spatial resolution ratio of

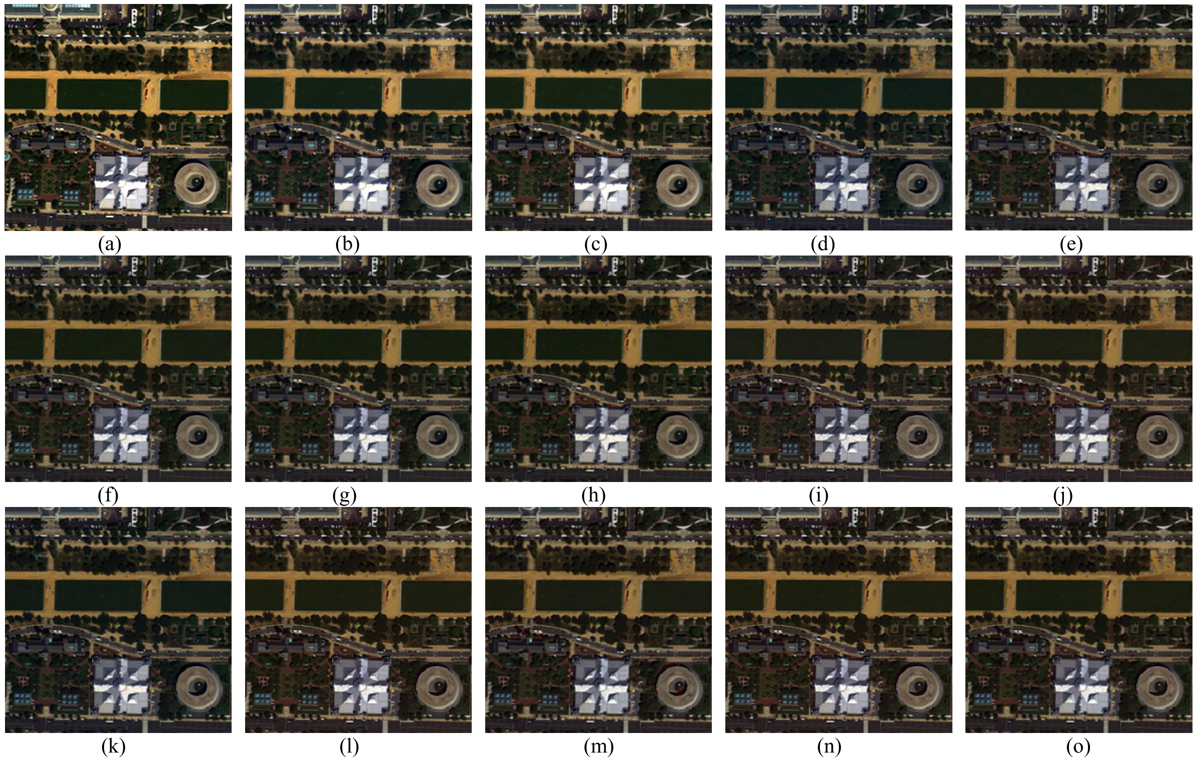

Fig. 15. Results of WorldView-2 sensor dataset at full resolution. (a) EXP. (b) BT-H. (c) C-GSA. (d) AWLP. (e) MTF-GLP. (f) MTF-GLP-FS. (g) MTF-GLP-CBD. (h) C-MTF-GLP-CBD. (i) MF. (j) MTF-GLP-HPM. (k). MTF-GLP-HPM-R. (l) MTF-GLP-HPM-H. (m) MTF-GLP-HPM-PP. (n) MTF-GLP-HPM-FS. (o) MTF-GLP-HPM-DS.

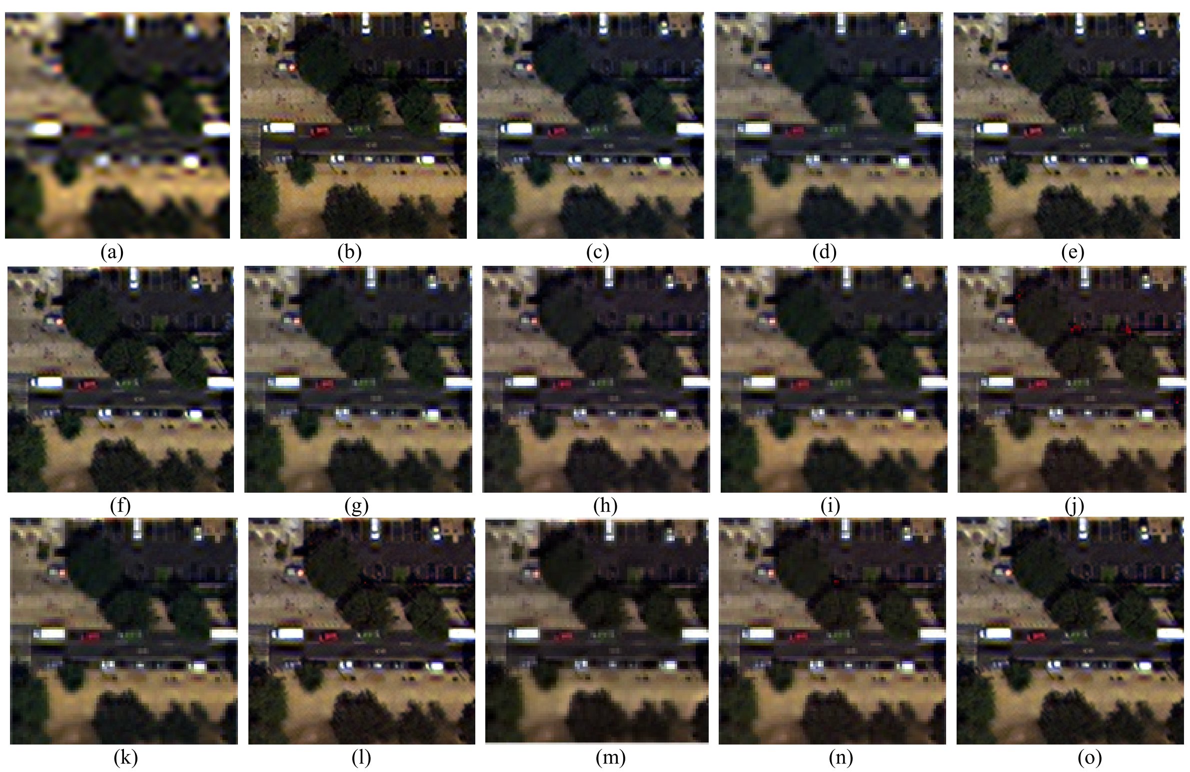

Fig. 16. Subareas of WorldView-2 sensor dataset at full resolution. (a) EXP. (b) BT-H. (c) C-GSA. (d) AWLP. (e) MTF-GLP. (f) MTF-GLP-FS. (g) MTF-GLP-CBD. (h) C-MTF-GLP-CBD. (i) MF. (j) MTF-GLP-HPM. (k). MTF-GLP-HPM-R. (l) MTF-GLP-HPM-H. (m) MTF-GLP-HPM-PP. (n) MTF-GLP-HPM-FS. (o) MTF-GLP-HPM-DS.

$R = 4$. The pansharpening result still has the same size as the original reference image [56]. The three evaluation indicators of the 15 methods at a reduced resolution are given in Tables VII and VIII.

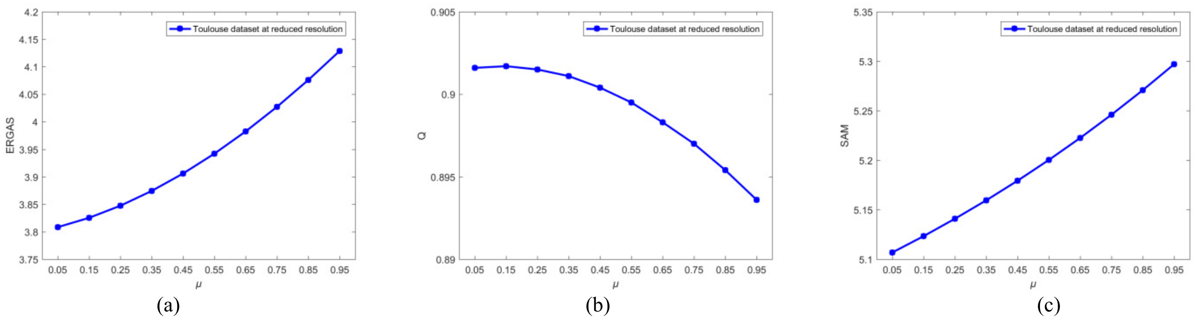

Fig. 17. (a) ERGAS, (b) Q-index, and (c) SAM evaluating at different μ for Toulouse dataset at reduced resolution.

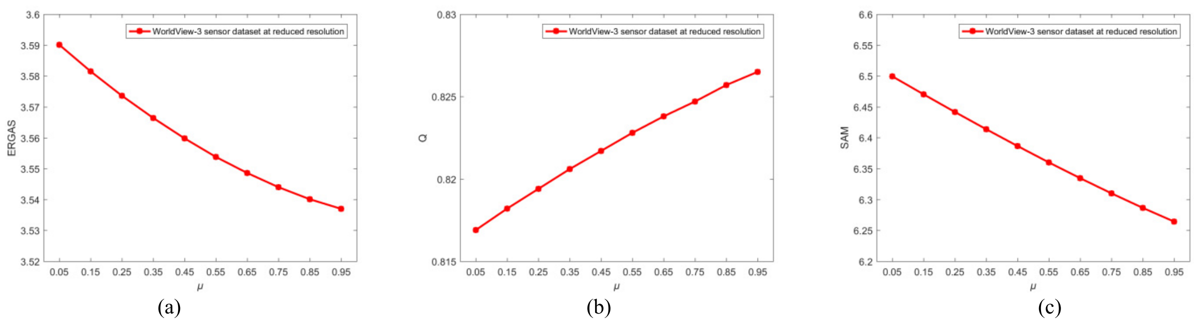

Fig. 18. (a) ERGAS, (b) Q-index, and (c) SAM evaluating at different μ for WorldView-3 sensor dataset at reduced resolution.

TABLE VII

ASSESSMENT FOR THE TOULOUSE DATASET OF 15 METHODS AT REDUCED RESOLUTION ($R = 2$)

	Q4	SAM	ERGAS
Reference	1.0000	0.0000	0.0000
EXP	0.8876	2.6160	7.0879
BT-H	0.9022	3.4394	8.1403
C-GSA	0.9060	4.2420	7.4354
AWLP	0.9135	4.1264	8.2869
MTF-GLP	0.9204	2.9081	7.1719
MTF-GLP-FS	0.9386	2.7952	5.9342
MTF-GLP-CBD	0.9368	2.8763	6.0394
C-MTF-GLP-CBD	0.9452	3.4686	5.5504
MF	0.9437	**2.4299**	6.0302
MTF-GLP-HPM	0.9253	2.5444	6.9112
MTF-GLP-HPM-R	0.9136	3.6958	7.8724
MTF-GLP-HPM-H	0.9377	3.0260	6.0368
MTF-GLP-HPM-PP	0.9217	3.1198	6.8027
MTF-GLP-HPM-FS	0.9393	2.9393	5.9480
MTF-GLP-HPM-DS	**0.9466**	2.8619	**5.4913**

TABLE VIII

ASSESSMENT FOR THE IKONOS SENSOR DATASET OF FIFTEEN METHODS AT REDUCED RESOLUTION ($R = 2$)

	Q4	SAM	ERGAS
Reference	1.0000	0.0000	0.0000
EXP	0.8335	0.9262	4.0893
BT-H	0.7944	1.1215	3.1648
C-GSA	0.7769	1.2416	3.4522
AWLP	0.8363	1.0038	3.0719
MTF-GLP	0.8365	1.0060	2.6033
MTF-GLP-FS	0.8480	0.9820	2.5825
MTF-GLP-CBD	0.8480	0.9816	2.5846
C-MTF-GLP-CBD	0.8260	1.1290	2.7352
MF	0.8303	1.0405	2.9886
MTF-GLP-HPM	0.8429	0.9141	2.3077
MTF-GLP-HPM-R	0.8516	0.9056	2.3064
MTF-GLP-HPM-H	0.8423	1.0169	2.4341
MTF-GLP-HPM-PP	0.8417	0.9298	2.5863
MTF-GLP-HPM-FS	0.8516	0.9056	2.3063
MTF-GLP-HPM-DS	**0.8517**	**0.9055**	**2.3058**

Based on the results presented in Tables VII and VIII, at $R = 2$, the proposed method shows a good performance on both datasets among all the compared methods. Therefore, the proposed method is suitable for MS with a different resolution.

B. Parameter μ

The parameter μ is introduced to balance the influence of fine M_b^{HR}, fine P^{HR}, and coarse P^{LR} on (22). Considering the aforementioned experimental results for the reduced resolution and full-resolution assessments, the parameter μ is vital for the MTF-GLP-HPM-DS method and makes the proposed method more flexible toward different sensors and imagery as compared to the other MRA methods. In this experiment, the impact of parameter μ is studied for different sensors and images scenarios. The three datasets for reduced resolution experiments include Toulouse dataset comprising buildings in an urban area, WorldView-3 sensor dataset comprising green vegetation in rural areas, and IKONOS sensor dataset comprising water in a suburban area. The two datasets used for full resolution experiments include QuickBird sensor dataset comprising water in a suburban area and WorldView-2 sensor dataset comprising buildings in an urban area. Therefore, we vary the parameter μ in the range of [0.05, 0.95] with a step size of 0.1 for three datasets used in reduced resolution experiments and two datasets used in full resolution experiments.

In the reduced resolution experiments, the ERGAS, Q-index, and SAM of the proposed method on the three datasets for $R = 4$ are shown in Figs. 17–19. As shown in Figs. 17(a)–19(a), the ERGAS value for Toulouse dataset

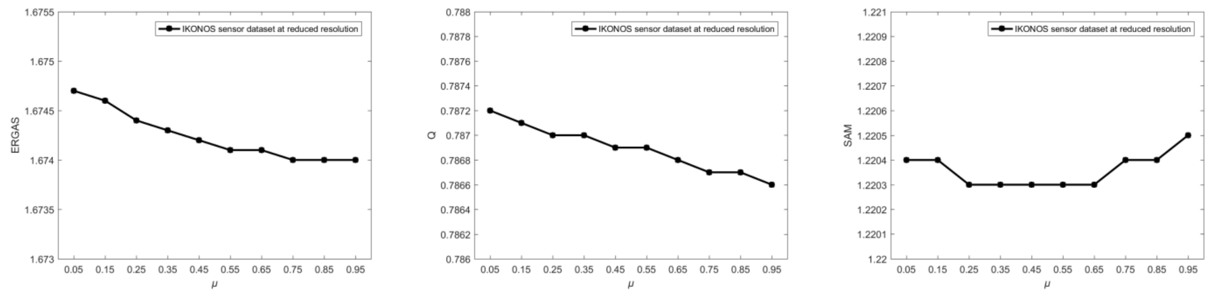

(a) (b) (c)

Fig. 19. (a) ERGAS, (b) Q-index, and (c) SAM evaluating at different μ for IKONOS sensor dataset at reduced resolution.

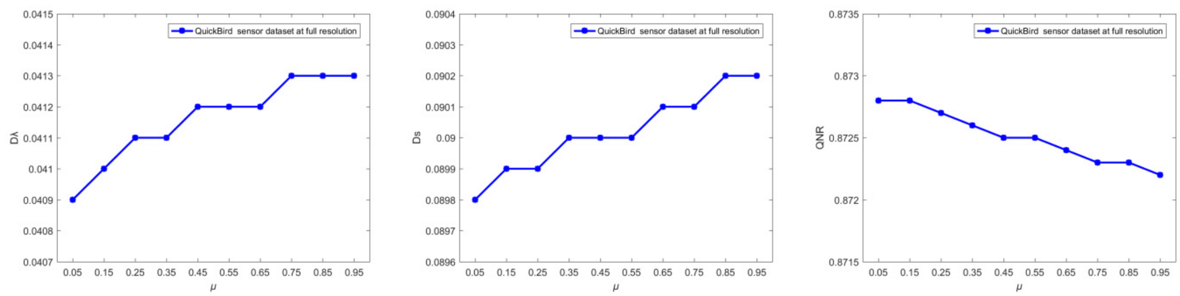

(a) (b) (c)

Fig. 20. (a) D_λ, (b) D_S, and (c) QNR evaluating at different μ for QuickBird sensor dataset at full resolution.

increases with μ, while it decreases for WorldView-3 and IKONOS sensor datasets. As shown in Figs. 17(b)–19(b), the Q-index value for Toulouse dataset and IKONOS sensor dataset decreases with μ, while it increases for WorldView-3 sensor dataset. As shown in Figs. 17(c)–19(c), the SAM value for Toulouse dataset increases with μ while it decreases for WorldView-3 sensor dataset and IKONOS sensor dataset. Thus, as the value of μ increases, the values of ERGAS and Q-index for Toulouse dataset became worse, but the value of SAM is improved. As compared to the WorldView-3 sensor dataset, the changes are opposite. The change for IKONOS sensor is not obvious as compared with the other two datasets. Considering that the proposed method achieves the best performance among all the methods, μ should be selected appropriately which made several indicators of the proposed method were better than those of the other 14 methods.

In the full resolution experiments, the values of D_λ, D_S, and QNR for different μ on the two datasets are shown in Figs. 20 and 21. As shown in Figs. 20 and 21, the value of μ should be as low as possible. This is because the better Q-index directly results in better D_λ, D_S, and QNR according to (34). Therefore, as the value of μ increases, the value of Q-index worsens. Thus, μ is set to 0.05 for the two datasets at full resolution to achieve good performance in terms of several indicators.

C. ERGAS for Different R

For IKONOS dataset evaluation performed in previous experiment, we conclude that a lower μ leads to a better Q-index and SAM, but worsens the ERGAS. To further illustrate this effect, we test the ERGAS maps for IKONOS sensor dataset at $R = 4$ and $R = 8$. As shown in Fig. 22, whether $R = 4$ and $R = 8$, the ERGAS decreases with an increase in μ. Thus, for two different R, the μ should be higher to obtain better ERGAS. For IKONOS dataset evaluation performed in previous experiment, the parameter μ is set to 0.5 by balancing the other indices to obtain the best pansharpening results.

TABLE IX

PROCESSING TIME OF THE PREVIOUS DATASETS OF 14 METHODS AT REDUCED RESOLUTION

	Toulouse	WorldView-3	IKONOS
BT-H	0.1198s	01263s	0.1193s
C-GSA	0.9131s	0.7720s	0.5233s
AWLP	0.1954s	0.2787s	0.2131s
MTF-GLP	0.4096s	0.6924s	0.4229s
MTF-GLP-FS	0.2171s	0.4261s	0.2142s
MTF-GLP-CBD	0.2057s	0.4873s	0.2018s
C-MTF-GLP-CBD	0.8699s	1.1324s	0.7872s
MF	0.2665s	0.3676s	0.2652s
MTF-GLP-HPM	0.3431s	0.7838s	0.3301s
MTF-GLP-HPM-R	0.2005s	0.3920s	0.2342s
MTF-GLP-HPM-H	0.2854s	0.5313s	0.2543s
MTF-GLP-HPM-PP	0.3881s	0.6846s	0.3441s
MTF-GLP-HPM-FS	0.1977s	0.3936s	0.1993s
MTF-GLP-HPM-DS	0.2627s	0.4278s	0.2324s

D. Processing Time

The processing time is another important evaluation index of the proposed method's performance. The processing time of the 14 pansharpening methods for the datasets at reduced and full resolutions are presented in Tables IX and X, respectively. As shown in Tables IX and X, although the execution time of the proposed method is not the shortest, the processing time of the proposed MTF-GLP-HPM-FS is relatively short as compared with the other MTF-GLP-HPM methods. MTF-GLP-HPM-DS method requires one more scale to consider than

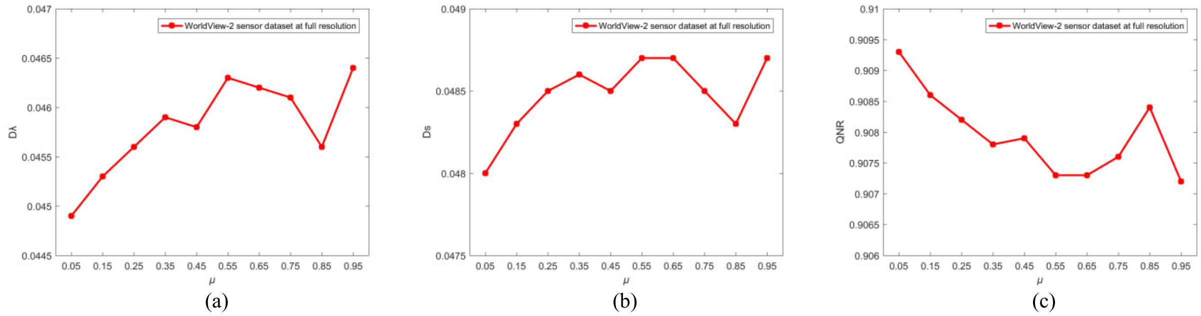

Fig. 21. (a) D_{λ}, (b) D_S, and (c) QNR evaluating at different μ for WorldView-2 sensor dataset at full resolution.

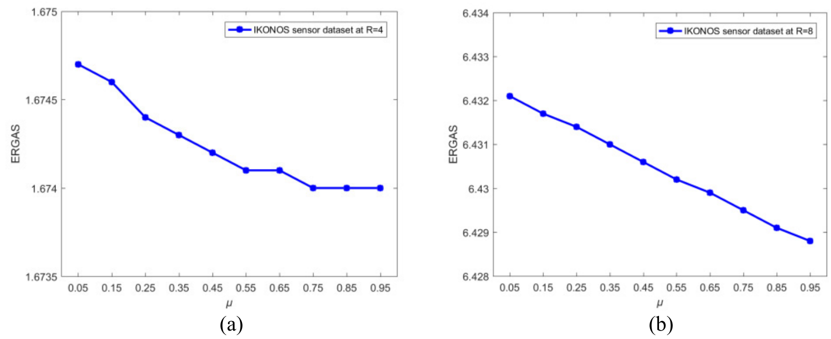

Fig. 22. ERGAS maps for IKONOS sensor dataset. (a) $R = 4$. (b) $R = 8$.

TABLE X

PROCESSING TIME OF THE PREVIOUS DATASETS OF FOURTEEN METHODS AT FULL RESOLUTION

	QuickBird	WorldView-2
BT-H	0.8674s	0.7799s
C-GSA	3.7031s	10.7593s
AWLP	3.3242s	4.7588s
MTF-GLP	2.5477s	6.1608s
MTF-GLP-FS	0.9946s	3.2501s
MTF-GLP-CBD	1.0837s	2.9076s
C-MTF-GLP-CBD	4.7031s	8.7207s
MF	1.4570s	1.8177s
MTF-GLP-HPM	1.9156s	4.6477s
MTF-GLP-HPM-R	1.2193s	3.8171s
MTF-GLP-HPM-H	1.6818s	3.4326s
MTF-GLP-HPM-PP	2.1757s	4.4590s
MTF-GLP-HPM-FS	1.0439s	2.7141s
MTF-GLP-HPM-DS	1.1478s	3.0216s

MTF-GLP-HPM-FS; thus, the proposed MTF-GLP-HPM-DS obtains an excellent result at the cost of a longer execution time.

E. Limitations

In this work, we build a dual-scale estimation of the HPM injection scheme model for regression based on MRA pansharpening method. It is worth noting that the manual adjustment of the parameter μ is accomplished based on many experiments. This means that any change in parameter μ requires us to modify the values and then again find the most suitable μ, which requires us to perform plenty of experiments. In addition, the accuracy of the parameters obtained by manual adjustment is not too high. Moreover, the processing time of the proposed method can be further improved using a simplified model.

V. CONCLUSION

In this work, we propose an MRA method for pansharpening based on dual-scale regression, which achieves a better pansharpening result as compared to various state-of-the-art MRA pansharpening methods. In the proposed method, an MRA model based on the scale regression is established. Then, this model is improved by adding the scale regression to the HPM injection scheme. The fine-scale information and coarse-scale information are integrated by the weight parameter and added to the scale regression to construct dual-scale regression, generating the final pansharpening result. The proposed method has two main advantages, including more scale information (fine-scale and coarse-scale information) for the scale regression and better adaptability toward different scenarios obtained by adjusting the weight parameter. The experimental results of the proposed method obtained using the two four-band datasets (the QuickBird and IKONOS datasets) and two eight-band datasets (the WorldView-2 and WorldView-3 datasets) demonstrate a good performance achieved within an acceptable time. The experimental results show that the performance of the proposed MTF-GLP-HPM-DS method is better for both the reduced and full-resolution assessments as compared to the other MRA methods.

In this work, an appropriate weight parameter μ is obtained experimentally. However, manual adjustment of parameter μ can be further improved, and the self-adaptability of this parameter can be considered in the future.

APPENDIX A

We show that the dual-scale regression model is iterative and convergent step by step. First, the initial injection coefficients g_b^0 are obtained for $M_b^{\mathrm{HR},0} = \hat{M}_b^{\mathrm{LR}}$ and are defined as

$$g_b^0 = \mu \frac{\mathrm{cov}\left(\hat{M}_b^{\mathrm{LR}}, P^{\mathrm{HR}}\right)}{\mathrm{var}\left(P^{\mathrm{HR}}\right)} + (1-\mu)\frac{\mathrm{cov}\left(\hat{M}_b^{\mathrm{LR}}, P^{\mathrm{LR}}\right)}{\mathrm{var}\left(P^{\mathrm{HR}}\right)}. \quad (35)$$

Then, g_b^1 can be expressed as follows:

$$\begin{aligned} g_b^1 &= \mu \frac{\mathrm{cov}\left(M_b^{\mathrm{HR},1}, P^{\mathrm{HR}}\right)}{\mathrm{var}\left(P^{\mathrm{HR}}\right)} + (1-\mu)\frac{\mathrm{cov}\left(M_b^{\mathrm{HR},1}, P^{\mathrm{LR}}\right)}{\mathrm{var}\left(P^{\mathrm{HR}}\right)} \\ &= \mu \frac{\mathrm{cov}\left(\hat{M}_b^{\mathrm{LR}} + g_b^0\left(P^{\mathrm{HR}} - P^{\mathrm{LR}}\right), P^{\mathrm{HR}}\right)}{\mathrm{var}\left(P^{\mathrm{HR}}\right)} \\ &\quad +(1-\mu)\frac{\mathrm{cov}\left(\hat{M}_b^{\mathrm{LR}} + g_b^0\left(P^{\mathrm{HR}} - P^{\mathrm{LR}}\right), P^{\mathrm{LR}}\right)}{\mathrm{var}\left(P^{\mathrm{HR}}\right)} \\ &= \left[\mu \frac{\mathrm{cov}\left(\hat{M}_b^{\mathrm{LR}}, P^{\mathrm{HR}}\right)}{\mathrm{var}\left(P^{\mathrm{HR}}\right)} + (1-\mu)\frac{\mathrm{cov}\left(\hat{M}_b^{\mathrm{LR}}, P^{\mathrm{LR}}\right)}{\mathrm{var}\left(P^{\mathrm{HR}}\right)}\right] \\ &\quad +\mu \frac{\mathrm{cov}\left(g_b^0\left(P^{\mathrm{HR}} - P^{\mathrm{LR}}\right), P^{\mathrm{HR}}\right)}{\mathrm{var}\left(P^{\mathrm{HR}}\right)} \\ &\quad +(1-\mu)\frac{\mathrm{cov}\left(g_b^0\left(P^{\mathrm{HR}} - P^{\mathrm{LR}}\right), P^{\mathrm{LR}}\right)}{\mathrm{var}\left(P^{\mathrm{HR}}\right)} \\ &= \left[\mu \frac{\mathrm{cov}\left(\hat{M}_b^{\mathrm{LR}}, P^{\mathrm{HR}}\right)}{\mathrm{var}\left(P^{\mathrm{HR}}\right)} + (1-\mu)\frac{\mathrm{cov}\left(\hat{M}_b^{\mathrm{LR}}, P^{\mathrm{LR}}\right)}{\mathrm{var}\left(P^{\mathrm{HR}}\right)}\right] \\ &\quad +\left\{\left[\mu \frac{\mathrm{cov}\left(\hat{M}_b^{\mathrm{LR}}, P^{\mathrm{HR}}\right)}{\mathrm{var}\left(P^{\mathrm{HR}}\right)} + (1-\mu)\frac{\mathrm{cov}\left(\hat{M}_b^{\mathrm{LR}}, P^{\mathrm{LR}}\right)}{\mathrm{var}\left(P^{\mathrm{HR}}\right)}\right] \cdot \left(1 - \frac{\mathrm{cov}\left(P^{\mathrm{HR}}, P^{\mathrm{LR}}\right)}{\mathrm{var}\left(P^{\mathrm{HR}}\right)}\right)\right\} \\ &= \left[\mu \frac{\mathrm{cov}\left(\hat{M}_b^{\mathrm{LR}}, P^{\mathrm{HR}}\right)}{\mathrm{var}\left(P^{\mathrm{HR}}\right)} + (1-\mu)\frac{\mathrm{cov}\left(\hat{M}_b^{\mathrm{LR}}, P^{\mathrm{LR}}\right)}{\mathrm{var}\left(P^{\mathrm{HR}}\right)}\right] \\ &\quad \cdot \left\{\left[1 - \frac{\mathrm{cov}\left(P^{\mathrm{HR}}, P^{\mathrm{LR}}\right)}{\mathrm{var}\left(P^{\mathrm{HR}}\right)}\right]^0 + \left[1 - \frac{\mathrm{cov}\left(P^{\mathrm{HR}}, P^{\mathrm{LR}}\right)}{\mathrm{var}\left(P^{\mathrm{HR}}\right)}\right]^1\right\} \\ &= \left[\mu \frac{\mathrm{cov}\left(\hat{M}_b^{\mathrm{LR}}, P^{\mathrm{HR}}\right)}{\mathrm{var}\left(P^{\mathrm{HR}}\right)} + (1-\mu)\frac{\mathrm{cov}\left(\hat{M}_b^{\mathrm{LR}}, P^{\mathrm{LR}}\right)}{\mathrm{var}\left(P^{\mathrm{HR}}\right)}\right] \\ &\quad \cdot \sum_{i=0}^{1}\left[1 - \frac{\mathrm{cov}\left(P^{\mathrm{HR}}, P^{\mathrm{LR}}\right)}{\mathrm{var}\left(P^{\mathrm{HR}}\right)}\right]^i. \end{aligned} \quad (36)$$

Thus, the expression of g_b^{n-1} is obtained as

$$\begin{aligned} g_b^{n-1} &= \left[\mu \frac{\mathrm{cov}\left(\hat{M}_b^{\mathrm{LR}}, P^{\mathrm{HR}}\right)}{\mathrm{var}\left(P^{\mathrm{HR}}\right)} + (1-\mu)\frac{\mathrm{cov}\left(\hat{M}_b^{\mathrm{LR}}, P^{\mathrm{LR}}\right)}{\mathrm{var}\left(P^{\mathrm{HR}}\right)}\right] \\ &\quad \cdot \sum_{i=0}^{n-1}\left[1 - \frac{\mathrm{cov}\left(P^{\mathrm{HR}}, P^{\mathrm{LR}}\right)}{\mathrm{var}\left(P^{\mathrm{HR}}\right)}\right]^i. \end{aligned} \quad (37)$$

Finally, to show that the dual-scale regression model is iterative and convergent, mathematical induction is used to obtain g_b^n derived from g_b^{n-1} in (30) as

$$\begin{aligned} g_b^n &= \mu \frac{\mathrm{cov}\left(M_b^{\mathrm{HR},n}, P^{\mathrm{HR}}\right)}{\mathrm{var}\left(P^{\mathrm{HR}}\right)} + (1-\mu)\frac{\mathrm{cov}\left(M_b^{\mathrm{HR},n}, P^{\mathrm{LR}}\right)}{\mathrm{var}\left(P^{\mathrm{HR}}\right)} \\ &= \left[\mu \frac{\mathrm{cov}\left(\hat{M}_b^{\mathrm{LR}}, P^{\mathrm{HR}}\right)}{\mathrm{var}\left(P^{\mathrm{HR}}\right)} + (1-\mu)\frac{\mathrm{cov}\left(\hat{M}_b^{\mathrm{LR}}, P^{\mathrm{LR}}\right)}{\mathrm{var}\left(P^{\mathrm{HR}}\right)}\right] \\ &\quad +\left\{\left[\mu \frac{\mathrm{cov}\left(\hat{M}_b^{\mathrm{LR}}, P^{\mathrm{HR}}\right)}{\mathrm{var}\left(P^{\mathrm{HR}}\right)} + (1-\mu)\frac{\mathrm{cov}\left(\hat{M}_b^{\mathrm{LR}}, P^{\mathrm{LR}}\right)}{\mathrm{var}\left(P^{\mathrm{HR}}\right)}\right] \cdot \sum_{i=0}^{n-1}\left[1 - \frac{\mathrm{cov}\left(P^{\mathrm{HR}}, P^{\mathrm{LR}}\right)}{\mathrm{var}\left(P^{\mathrm{HR}}\right)}\right]^i\right\} \\ &\quad \cdot \frac{\mathrm{cov}\left(\left(P^{\mathrm{HR}} - P^{\mathrm{LR}}\right), P^{\mathrm{LR}}\right)}{\mathrm{var}\left(P^{\mathrm{HR}}\right)} \\ &= \left[\mu \frac{\mathrm{cov}\left(\hat{M}_b^{\mathrm{LR}}, P^{\mathrm{HR}}\right)}{\mathrm{var}\left(P^{\mathrm{HR}}\right)} + (1-\mu)\frac{\mathrm{cov}\left(\hat{M}_b^{\mathrm{LR}}, P^{\mathrm{LR}}\right)}{\mathrm{var}\left(P^{\mathrm{HR}}\right)}\right] \\ &\quad \cdot \sum_{i=0}^{n}\left[1 - \frac{\mathrm{cov}\left(P^{\mathrm{HR}}, P^{\mathrm{LR}}\right)}{\mathrm{var}\left(P^{\mathrm{HR}}\right)}\right]^i. \end{aligned} \quad (38)$$

Similarly, the iterative process used in the regression requires a fixed point when n approaches infinity. Therefore, g_b^{∞} is defined as follows:

$$\begin{aligned} g_b^{\infty} &= \lim_{n\to\infty} g_b^n \\ &= \left[\mu \frac{\mathrm{cov}\left(\hat{M}_b^{\mathrm{LR}}, P^{\mathrm{HR}}\right)}{\mathrm{var}\left(P^{\mathrm{HR}}\right)} + (1-\mu)\frac{\mathrm{cov}\left(\hat{M}_b^{\mathrm{LR}}, P^{\mathrm{LR}}\right)}{\mathrm{var}\left(P^{\mathrm{HR}}\right)}\right] \\ &\quad \cdot \sum_{i=0}^{\infty}\left[1 - \frac{\mathrm{cov}\left(P^{\mathrm{HR}}, P^{\mathrm{LR}}\right)}{\mathrm{var}\left(P^{\mathrm{HR}}\right)}\right]^i. \end{aligned} \quad (39)$$

Particularly, due to the fact that

$$0 < \left|1 - \frac{\mathrm{cov}\left(P^{\mathrm{HR}}, P^{\mathrm{LR}}\right)}{\mathrm{var}\left(P^{\mathrm{HR}}\right)}\right| < 1. \quad (40)$$

We have

$$\begin{aligned} g_b^{\infty} &= \left[\mu \frac{\mathrm{cov}\left(\hat{M}_b^{\mathrm{LR}}, P^{\mathrm{HR}}\right)}{\mathrm{var}\left(P^{\mathrm{HR}}\right)} + (1-\mu)\frac{\mathrm{cov}\left(\hat{M}_b^{\mathrm{LR}}, P^{\mathrm{LR}}\right)}{\mathrm{var}\left(P^{\mathrm{HR}}\right)}\right] \cdot \frac{1}{1 - \left[1 - \frac{\mathrm{cov}\left(P^{\mathrm{HR}}, P^{\mathrm{LR}}\right)}{\mathrm{var}\left(P^{\mathrm{HR}}\right)}\right]} \\ &= \left[\mu \frac{\mathrm{cov}\left(\hat{M}_b^{\mathrm{LR}}, P^{\mathrm{HR}}\right)}{\mathrm{var}\left(P^{\mathrm{HR}}\right)} + (1-\mu)\frac{\mathrm{cov}\left(\hat{M}_b^{\mathrm{LR}}, P^{\mathrm{LR}}\right)}{\mathrm{var}\left(P^{\mathrm{HR}}\right)}\right] \cdot \frac{1}{\frac{\mathrm{cov}\left(P^{\mathrm{HR}}, P^{\mathrm{LR}}\right)}{\mathrm{var}\left(P^{\mathrm{HR}}\right)}} \\ &= \mu \frac{\mathrm{cov}\left(\hat{M}_b^{\mathrm{LR}}, P^{\mathrm{HR}}\right)}{\mathrm{cov}\left(P^{\mathrm{HR}}, P^{\mathrm{LR}}\right)} + (1-\mu)\frac{\mathrm{cov}\left(\hat{M}_b^{\mathrm{LR}}, P^{\mathrm{LR}}\right)}{\mathrm{cov}\left(P^{\mathrm{HR}}, P^{\mathrm{LR}}\right)}. \end{aligned} \quad (41)$$

REFERENCES

[1] M. Schmitt and X. X. Zhu, "Data fusion and remote sensing: An ever-growing relationship," *IEEE Geosci. Remote Sens. Mag.*, vol. 4, no. 4, pp. 6–23, Dec. 2016.

[2] S. Mei, Y. Geng, J. Hou, and Q. Du, "Learning hyperspectral images from RGB images via a coarse-to-fine CNN," *Sci. China Inf. Sci.*, vol. 65, no. 5, May 2022, Art. no. 152102.

[3] Z. Tan, M. Gao, X. Li, and L. Jiang, "A flexible reference-insensitive spatiotemporal fusion model for remote sensing images using conditional generative adversarial network," *IEEE Trans. Geosci. Remote Sens.*, early access, Jan. 26, 2021, doi: 10.1109/TGRS.2021.3050551.

[4] R. Gharbia, A. H. E. Baz, A. E. Hassanien, and M. Tolba, "Remote sensing image fusion approach based on Brovey and wavelets transforms," in *Proc. 5th Int. Conf. Innov. Bio-Inspired Comput. Appl. (IBICA)*, vol. 303, 2014, pp. 311–321.

[5] S. Mei, J. Ji, Y. Geng, Z. Zhang, X. Li, and Q. Du, "Unsupervised spatial–spectral feature learning by 3D convolutional autoencoder for hyperspectral classification," *IEEE Trans. Geosci. Remote Sens.*, vol. 57, no. 9, pp. 6808–6820, Apr. 2019.

[6] X. Li, L. Wang, Q. Cheng, P. Wu, W. Gan, and L. Fang, "Cloud removal in remote sensing images using nonnegative matrix factorization and error correction," *ISPRS J. Photogramm. Remote Sens.*, vol. 148, pp. 103–113, Feb. 2019.

[7] S. Mei, X. Li, X. Liu, H. Cai, and Q. Du, "Hyperspectral image classification using attention-based bidirectional long short-term memory network," *IEEE Trans. Geosci. Remote Sens.*, early access, Aug. 11, 2021, doi: 10.1109/TGRS.2021.3102034.

[8] G. Vivone *et al.*, "A new benchmark based on recent advances in multispectral pansharpening: Revisiting pansharpening with classical and emerging pansharpening methods," *IEEE Geosci. Remote Sens. Mag.*, vol. 9, no. 1, pp. 53–81, Mar. 2021.

[9] P. Liu, M. Wang, L. Wang, and W. Han, "Remote-sensing image denoising with multi-sourced information," *IEEE J. Sel. Topics Appl. Earth Observ. Remote Sens.*, vol. 12, no. 2, pp. 660–674, Feb. 2019.

[10] G. Vivone *et al.*, "A critical comparison among pansharpening algorithms," *IEEE Trans. Geosci. Remote Sens.*, vol. 53, no. 5, pp. 2565–2586, May 2015.

[11] G. Vivone, R. Restaino, G. Licciardi, M. Dalla Mura, and J. Chanussot, "MultiResolution analysis and component substitution techniques for hyperspectral pansharpening," in *Proc. IEEE Geosci. Remote Sens. Symp.*, Jul. 2014, pp. 2649–2652.

[12] F. Laporterie-Déjean, H. de Boissezon, G. Flouzat, and M.-J. Lefèvre-Fonollosa, "Thematic and statistical evaluations of five panchromatic/multispectral fusion methods on simulated PLEIADES-HR images," *Inf. Fusion*, vol. 6, no. 3, pp. 193–212, Sep. 2005.

[13] X. X. Zhu *et al.*, "Deep learning in remote sensing: A comprehensive review and list of resources," *IEEE Geosci. Remote Sens. Mag.*, vol. 5, no. 4, pp. 8–36, Dec. 2017.

[14] W. J. Carper, T. M. Lillesand, and R. W. Kiefer, "The use of intensity-hue-saturation transformations for merging SPOT panchromatic and multispectral image data," *Photogramm. Eng. Remote Sens.*, vol. 56, no. 4, pp. 459–467, Apr. 1990.

[15] P. S. Chavez and A. W. Kwarteng, "Extracting spectral contrast in landsat thematic mapper image data using selective principal component analysis," *Photogramm. Eng. Remote Sens.*, vol. 55, no. 3, pp. 339–348, Mar. 1989.

[16] C. A. Laben and B. V. Brower, "Process for enhancing the spatial resolution of multispectral imagery using pan-sharpening," U.S. Patent 6011875, Jan. 4, 2000.

[17] B. Aiazzi, S. Baronti, and M. Selva, "Improving component substitution pansharpening through multivariate regression of MS+Pan data," *IEEE Trans. Geosci. Remote Sens.*, vol. 45, no. 10, pp. 3230–3239, Oct. 2007.

[18] G. Masi, D. Cozzolino, L. Verdoliva, and G. Scarpa, "Pansharpening by convolutional neural networks," *Remote Sens.*, vol. 8, no. 7, p. 594, Jul. 2016.

[19] Y. Wei and Q. Yuan, "Deep residual learning for remote sensed imagery pansharpening," in *Proc. Int. Workshop Remote Sens. Intell. Process. (RSIP)*, May 2017, pp. 1–4.

[20] S. Mei, X. Chen, Y. Zhang, J. Li, and A. Plaza, "Accelerating convolutional neural network-based hyperspectral image classification by step activation quantization," *IEEE Trans. Geosci. Remote Sens.*, early access, Feb. 24, 2021, doi: 10.1109/TGRS.2021.3058321.

[21] Y. Wei, Q. Yuan, H. Shen, and L. Zhang, "Boosting the accuracy of multispectral image pansharpening by learning a deep residual network," *IEEE Geosci. Remote Sens. Lett.*, vol. 14, no. 10, pp. 1795–1799, Oct. 2017.

[22] J. Yang, X. Fu, Y. Hu, Y. Huang, X. Ding, and J. Paisley, "PanNet: A deep network architecture for pan-sharpening," in *Proc. IEEE Int. Conf. Comput. Vis. (ICCV)*, Oct. 2017, pp. 1753–1761.

[23] Z. Shao and J. Cai, "Remote sensing image fusion with deep convolutional neural network," *IEEE J. Sel. Topics Appl. Earth Observ. Remote Sens.*, vol. 11, no. 5, pp. 1656–1669, May 2018.

[24] W. Yao, Z. Zeng, C. Lian, and H. Tang, "Pixel-wise regression using U-Net and its application on pansharpening," *Neurocomputing*, vol. 312, pp. 364–371, Oct. 2018.

[25] L. Mu, L. Wang, Y. Wang, X. Chen, and W. Han, "Urban land use and land cover change prediction via self-adaptive cellular based deep learning with multisourced data," *IEEE J. Sel. Topics Appl. Earth Observ. Remote Sens.*, vol. 12, no. 12, pp. 5233–5247, Dec. 2019.

[26] Y. Zhang, C. Liu, M. Sun, and Y. Ou, "Pan-sharpening using an efficient bidirectional pyramid network," *IEEE Trans. Geosci. Remote Sens.*, vol. 57, no. 8, pp. 5549–5563, Aug. 2019.

[27] H. Li, R. Feng, L. Wang, Y. Zhong, and L. Zhang, "Superpixel-based reweighted low-rank and total variation sparse unmixing for hyperspectral remote sensing imagery," *IEEE Trans. Geosci. Remote Sens.*, vol. 59, no. 1, pp. 629–647, Jan. 2021.

[28] Q. Wang, Y. Tang, and P. M. Atkinson, "The effect of the point spread function on downscaling continua," *ISPRS J. Photogramm. Remote Sens.*, vol. 168, pp. 251–267, Oct. 2020.

[29] Q. Wang, W. Shi, and P. M. Atkinson, "Information loss-guided multi-resolution image fusion," *IEEE Trans. Geosci. Remote Sens.*, vol. 58, no. 1, pp. 45–57, Jan. 2020.

[30] X. Otazu, M. González-Audícana, O. Fors, and J. Núñez, "Introduction of sensor spectral response into image fusion methods. Application to wavelet-based methods," *IEEE Trans. Geosci. Remote Sens.*, vol. 43, no. 10, pp. 2376–2385, Oct. 2005.

[31] J. G. Liu, "Smoothing filter-based intensity modulation: A spectral preserve image fusion technique for improving spatial details," *Int. J. Remote Sens.*, vol. 21, no. 18, pp. 3461–3472, Dec. 2000.

[32] R. Restaino, G. Vivone, M. Dalla Mura, and J. Chanussot, "Fusion of multispectral and panchromatic images based on morphological operators," *IEEE Trans. Image Process.*, vol. 25, no. 6, pp. 2882–2895, Jun. 2016.

[33] B. Aiazzi, L. Alparone, S. Baronti, A. Garzelli, and M. Selva, "MTF-tailored multiscale fusion of high-resolution MS and PAN imagery," *Photogramm. Eng. Remote Sens.*, vol. 72, no. 5, pp. 591–596, May 2006.

[34] L. Alparone, L. Wald, J. Chanussot, C. Thomas, P. Gamba, and L. M. Bruce, "Comparison of pansharpening algorithms: Outcome of the 2006 GRS-S data fusion contest," *IEEE Trans. Geosci. Remote Sens.*, vol. 45, no. 10, pp. 3012–3021, Oct. 2007.

[35] R. Restaino, M. D. Mura, G. Vivone, and J. Chanussot, "Context-adaptive pansharpening based on image segmentation," *IEEE Trans. Geosci. Remote Sens.*, vol. 55, no. 2, pp. 753–766, Feb. 2017.

[36] G. Vivone, R. Restaino, M. Dalla Mura, G. Licciardi, and J. Chanussot, "Contrast and error-based fusion schemes for multispectral image pansharpening," *IEEE Geosci. Remote Sens. Lett.*, vol. 11, no. 5, pp. 930–934, May 2014.

[37] B. Aiazzi, L. Alparone, S. Baronti, A. Garzelli, and M. Selva, "An MTF-based spectral distortion minimizing model for pan-sharpening of very high resolution multispectral images of urban areas," in *Proc. 2nd GRSS/ISPRS Joint Workshop Remote Sens. Data Fusion Over Urban Areas*, May 2003, pp. 90–94.

[38] S. Lolli, L. Alparone, A. Garzelli, and G. Vivone, "Haze correction for contrast-based multispectral pansharpening," *IEEE Geosci. Remote Sens. Lett.*, vol. 14, no. 12, pp. 2255–2259, Dec. 2017.

[39] J. Lee and C. Lee, "Fast and efficient panchromatic sharpening," *IEEE Trans. Geosci. Remote Sens.*, vol. 48, no. 1, pp. 155–163, Jan. 2010.

[40] R. D. Cook and S. Weisberg, "Criticism and influence analysis in regression," *Sociol. Methodol.*, vol. 13, pp. 313–361, 1982.

[41] G. Vivone, R. Restaino, and J. Chanussot, "Full scale regression-based injection coefficients for panchromatic sharpening," *IEEE Trans. Image Process.*, vol. 27, no. 7, pp. 3418–3431, Jul. 2018.

[42] G. Vivone, R. Restaino, and J. Chanussot, "A regression-based high-pass modulation pansharpening approach," *IEEE Trans. Geosci. Remote Sens.*, vol. 56, no. 2, pp. 984–996, Feb. 2018.

[43] R. A. Schowengerdt, *Remote Sensing: Models and Methods for Image Processing*, 2nd ed. Orlando, FL, USA: Academic, 1997.

[44] Q. Wang, Y. Tang, X. Tong, and P. M. Atkinson, "Virtual image pair-based spatio-temporal fusion," *Remote Sens. Environ.*, vol. 249, Nov. 2020, Art. no. 112009.

[45] D. M. Zhang and X. D. Zhang, "Pansharpening through proportional detail injection based on generalized relative spectral response," *IEEE Geosci. Remote Sens. Lett.*, vol. 8, no. 5, pp. 978–982, Sep. 2011.

[46] L. Wald, T. Ranchin, and M. Mangolini, "Fusion of satellite images of different spatial resolutions: Assessing the quality of resulting images," *Photogramm. Eng. Remote Sens.*, vol. 63, no. 6, pp. 691–699, 1997.

[47] Q. Wang, X. Ding, X. Tong, and P. M. Atkinson, "Spatio-temporal spectral unmixing of time-series images," *Remote Sens. Environ.*, vol. 259, Jun. 2021, Art. no. 112407.

[48] L. Wald, *Data Fusion: Definitions and Architectures-Fusion of Images of Different Spatial Resolutions*. Paris, France: Les Presses de l'École des Mines, 2002.

[49] R. H. Yuhas, A. F. H. Goetz, and J. W. Boardman, "Discrimination among semi-arid landscape endmembers using the spectral angle mapper (SAM) algorithm," in *Proc. Summaries 3rd Annu. JPL Airborne Geosci. Workshop*, 1992, pp. 147–149.

[50] Z. Wang and A. C. Bovik, "A universal image quality index," *IEEE Signal Process. Lett.*, vol. 9, no. 3, pp. 81–84, Mar. 2002.

[51] L. Alparone, B. Aiazzi, S. Baronti, A. Garzelli, F. Nencini, and M. Selva, "Multispectral and panchromatic data fusion assessment without reference," *Photogramm. Eng. Remote Sens.*, vol. 74, no. 2, pp. 193–200, Feb. 2008.

[52] X. Meng *et al.*, "A large-scale benchmark data set for evaluating pansharpening performance: Overview and implementation," *IEEE Geosci. Remote Sens. Mag.*, vol. 9, no. 1, pp. 18–52, Mar. 2021.

[53] B. Aiazzi *et al.*, "Effects of multitemporal scene changes on pansharpening fusion," in *Proc. 6th Int. Workshop Anal. Multi-Temporal Remote Sens. Images (Multi-Temp)*, Jul. 2011, pp. 73–76.

[54] P. Wang, L. Wang, H. Leung, and G. Zhang, "Super-resolution mapping based on spatial–spectral correlation for spectral imagery," *IEEE Trans. Geosci. Remote Sens.*, vol. 59, no. 3, pp. 2256–2268, Mar. 2021.

[55] T. Updike and C. Comp, "Radiometric use of WorldView-2 imagery," Tech. Note, Digit. Globe, Longmont, CO, USA, 2010, pp. 1–17.

[56] J. Marcello, E. Ibarrola-Ulzurrun, C. Gonzalo-Martin, J. Chanussot, and G. Vivone, "Assessment of hyperspectral sharpening methods for the monitoring of natural areas using multiplatform remote sensing imagery," *IEEE Trans. Geosci. Remote Sens.*, vol. 57, no. 10, pp. 8208–8222, Oct. 2019.

Peng Wang (Member, IEEE) received the B.E. and Ph.D. degrees from the College of Information and Communications Engineering, Harbin Engineering University, Harbin, China, in 2012 and 2018, respectively.

He is currently an Associate Professor with the College of Electronic and Information Engineering, Nanjing University of Aeronautics and Astronautics, Nanjing, Jiangsu, China. He has authored one book about sub-pixel mapping and more than 50 articles. His research interests include remote-sensing imagery processing and machine learning.

Hongyu Yao received the B.E. degree in electronic information engineering from the Xi'an University of Posts and Telecommunications, Xi'an, China, in 2020. She is currently pursuing the M.S. degree with the College of Electronic and Information Engineering, Nanjing University of Aeronautics and Astronautics.

Her research interest includes remote-sensing image processing.

Cai Li received the Ph.D. degree in marine environment monitoring technology from the South China Sea Institute of Oceanology, Chinese Academy of Sciences, Guangzhou, China, in 2006.

Since 2012, she has been working with Marine Environmental Monitoring Technology, South China Sea Institute of Oceanology, Chinese Academy of Sciences, where she is currently a Researcher. Her research interests include marine environment monitoring technology, ecological Internet of Things technology and engineering, and water optical and biochemical element measurement technology and application.

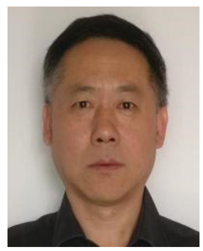

Gong Zhang (Member, IEEE) received the Ph.D. degree in electronic engineering from the Nanjing University of Aeronautics and Astronautics (NUAA), Nanjing, China, in 2002.

From 1990 to 1998, he was a Member of Technical Staff at the No724 Institute of China Shipbuilding Industry Corporation, Nanjing. Since 1998, he has been working with the College of Electronics and Information Engineering, NUAA, where he is currently a Professor. His research interests include radar signal processing and compressive sensing.

Dr. Zhang is a member of the Committee of Electromagnetic Information, Chinese Society of Astronautics, and a Senior Member of the Chinese Institute of Electronics.

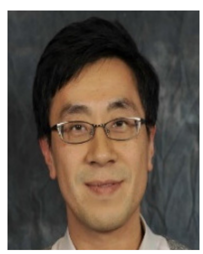

Henry Leung (Fellow, IEEE) received the Ph.D. degree in electrical and computer engineering from McMaster University, Hamilton, ON, Canada, in 1991.

He is currently a Professor with the Department of Electrical and Computer Engineering, University of Calgary, Calgary, AB, Canada. Before joining the University of Calgary, he worked with the Department of National Defense (DND) of Canada as the Defense Scientist. His research interests include information fusion, machine learning, IoT, nonlinear dynamics, robotics, and signal and image processing.

Dr. Leung is an Associate Editor of the *IEEE Circuits and Systems Magazine*. He is the Topic Editor on "Robotic Sensors" of the *International Journal of Advanced Robotic Systems*. He is also an Editor of the book series on *Information Fusion and Data Science* (Springer). In addition, he is a fellow of SPIE.